MICROBIOLOGY

Phosphorylation of shiftless is important for inhibiting the programmed −1 ribosomal frameshift

Yueli Zhang[1,2,3,4]†, Zhijian Li[1,2,3,4]*†, Huihui Chong[1,2,3,4], Pengjiao Hou[1,2,3,4,5], Wei Hao[1,2,3,4], Mengyun Li[1,2,3,4], Zhicheng Liu[6], Wei Jia[6], Bo Qin[1,2,3,4], Yuxian He[1,2,3,4]*, Sheng Cui[1,2,3,4]*

Shiftless (SFL) is a broad-spectrum inhibitor of programmed −1 ribosomal frameshift (−1 PRF) and exhibits various antiviral activities. Here, we characterized human SFL structurally and biochemically. The 2.0-angstrom resolution crystal structure of SFL reveals a boat-like module comprising an N-terminal helical bundle and three zinc fingers at the C terminus. A hyperphosphorylation loop (HPL) buried between the helical bundle and the zinc finger 1 harbors four phosphorylated residues (p-S249, p-T250 p-T253, and p-S256), which are important to protein folding. SFL forms monomers in solution and binds the HIV-1 −1 PRF sequence with nanomolar affinity (K_D = 5.7 nanomolar). Disruption of HPL phosphorylation decreased the RNA binding affinity and undermined the SFL-mediated −1 PRF inhibition of various viruses. Proximity-dependent biotinylation identified three cellular Ser/Thr kinases—EEF2K, NEK9, and PBK—that phosphorylate SFL in cells. These findings shed light on the mechanisms underlying −1 PRF regulation by SFL and provide insights into the role of SFL in virus inhibition.

INTRODUCTION

Human shiftless (denoted as SFL throughout this paper), also known as C19orf66, is an interferon (IFN)–stimulated gene. It bears many other aliases, including FLJ11286, IRAV (IFN-regulated antiviral gene) and RyDEN (Repressor of yield of dengue virus DENV), based on identification of its antiviral activities (*1*–*3*). The protein was most recently named "Shiftless" because it acts as a broad inhibitor of the programmed −1 ribosomal frameshift (−1 PRF) used by viruses, which is exemplified by HIV-1 (*2*).

SFL also inhibits a wide range of other viruses including flaviviruses such as dengue virus (DENV), West Nile virus (WNV), Zika virus (ZIKV), Japanese encephalitis virus (JEV), and yellow fever virus (YFV) (*3*–*6*). Molecular mechanisms underlying SFL-mediated antiviral activity are multifaceted. SFL inhibits DENV and WNV protein translation via binding with two mRNA binding proteins poly(A)-binding protein cytoplasmic 1 (PABPC1) and La motif-related protein 1 (LARP1) (*3*). SFL binds RNAs and interacts with two RNA decay-related proteins MOV10 and UPF1, indicating a role in viral RNA destabilization (*7*). SFL suppresses ZIKV replication by inducing degradation of viral protein NS3 through a lysosome-dependent pathway (*6*). Mouse SFL is an ortholog of human SFL, which restricts the replication of hepatitis C virus (HCV) and rodent hepacivirus (RHV) through interaction with the double-stranded RNA (dsRNA) intermediates within the viral replication factory (*8*). SFL also inhibits viral RNA replication of ZIKV, DENV, YFV, and HCV following initial viral protein translation, and mouse SFL affects ZIKV-induced neurological disease in mice (*4*).

One of the best-characterized antiviral mechanisms of SFL is the inhibition of the −1 PRF, a recoding mechanism in mRNA translation that is exploited by viruses to increase their coding capacity (*9*). SFL recognizes the −1 PRF signal in viral RNAs and binds to translating ribosomes, which ultimately causes premature translation termination, thereby inhibiting viral protein production. For example, SFL recognizes the −1 PRF signal in the HIV-1 genome, leading to inhibition of the Gag-Pol protein expression (*2*); in addition, they also found that SFL could inhibit many different −1 PRF signals encoded by both viruses and cellular genes (*2*). SFLS, the isoform 4 of SFL inactive in −1 PRF inhibition, lacks 36 amino acids (residue 164 to 199); it has been reported that this region of SFL is essential for RNA binding and ribosome association (*2*, *10*). In addition, alanine scanning mutagenesis shows that basic amino acids in predicted zinc finger of SFL are essential for the suppression of Gag-Pol expression (*11*). Likewise, SFL targets the −1 PRF signal between codons 8 and 9 in the JEV NS2A sequence, inhibiting the expression of NS1′ (*5*). SFL also suppresses the −1 PRF between the orf1a and orf1b genes of severe acute respiratory syndrome coronavirus 2 (SARS-CoV-2) to inhibit the translation of orf1b (*12*).

RESULTS

Biochemical characterization of human SFL

To gain molecular insights into SFL-mediated inhibition of the −1 PRF, we performed biochemical characterization of SFL. Few conserved domains could be identified from this 291–amino acid protein, except for a zinc finger domain (*13*). SFL is highly conserved from zebrafish to humans (fig. S1), underscoring its important role in vertebrates. We ectopically expressed an N-terminal 6×His-tagged full-length SFL in high-five insect cells. The His-tag was cleaved using tobacco etch virus (TEV) proteinase before subsequent experiments (Fig. 1A). We conducted analytical ultracentrifugation of the lastly purified SFL (Fig. 1B), and the calculated molecular mass was 35.0 kDa, which is slightly higher than the theoretical molecular mass of 33.0 kDa. This indicates that SFL is

[1]NHC Key Laboratory of Systems Biology of Pathogens, National Institute of Pathogen Biology, Chinese Academy of Medical Sciences & Peking Union Medical College, Beijing, China. [2]Key Laboratory of Pathogen Infection Prevention and Control (Ministry of Education), National Institute of Pathogen Biology, Chinese Academy of Medical Sciences & Peking Union Medical College, Beijing, China. [3]State Key Laboratory of Respiratory Health and Multimorbidity, National Institute of Pathogen Biology, Chinese Academy of Medical Sciences & Peking Union Medical College, Beijing, China. [4]National Institute of Pathogen Biology and Center for AIDS Research, Chinese Academy of Medical Sciences & Peking Union Medical College, Beijing, China. [5]Beijing Institute of Hepatology, Beijing Youan Hospital, Capital Medical University, Beijing, China. [6]Vivomass Biotech Co. Ltd., Suzhou, China.
*Corresponding author. Email: lizhijian@ipbcams.ac.cn (Z.L.); yhe@ipb.pumc.edu.cn (Y.H.); cui.sheng@ipb.pumc.edu.cn (S.C.)
†These authors contributed equally to this work.

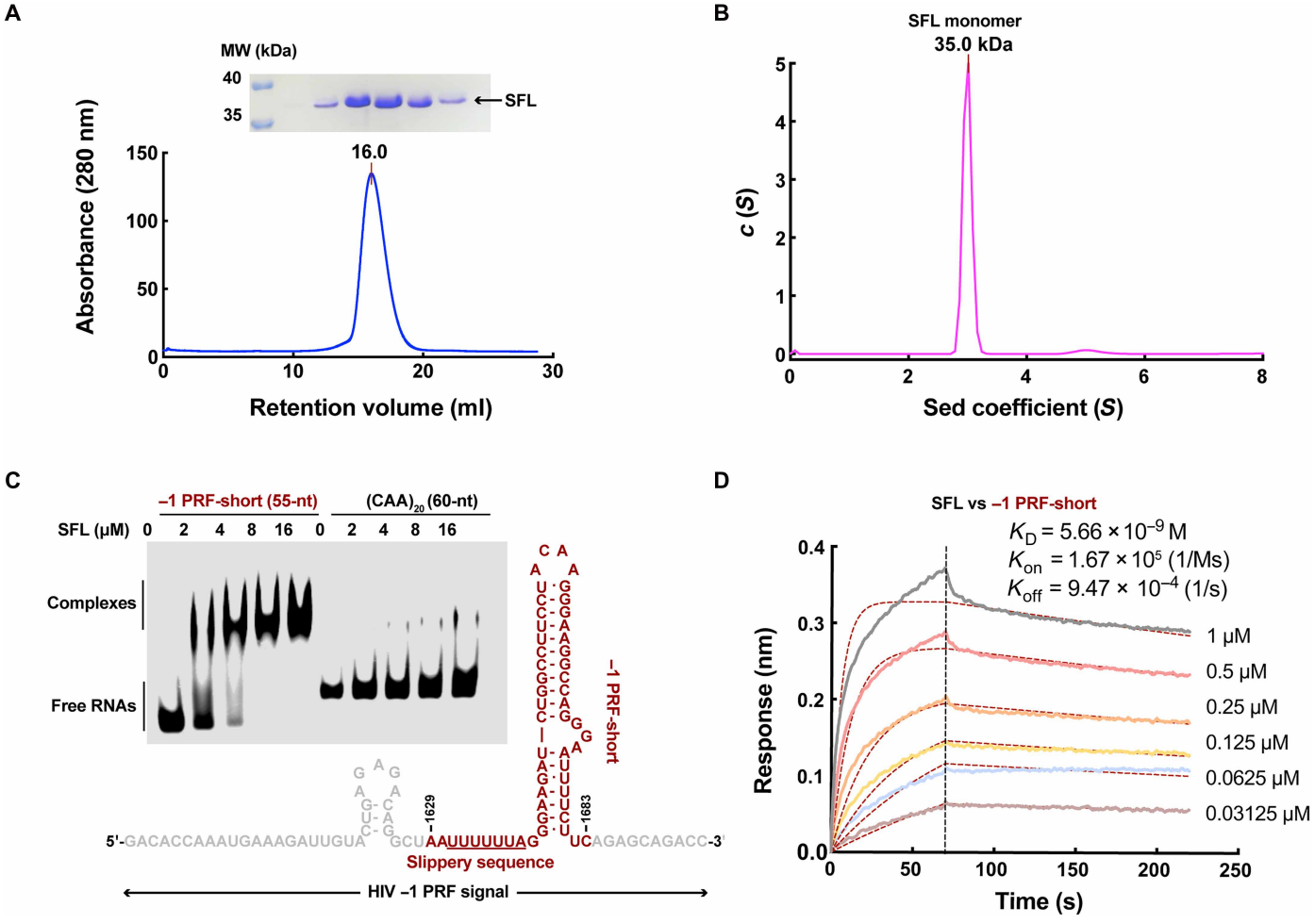

Fig. 1. Biochemical characterization of recombinant human SFL. (**A**) Final purification of human SFL by size exclusion chromatography. Top inset: SDS-PAGE analysis of the peak fractions from the eluate. MW, molecular weight standards. (**B**) Analytical ultracentrifugation of the purified SFL protein. The calculated molecular mass is shown on top of the peak. (**C**) Top left: EMSAs for the interaction of SFL with different RNA substrates. −1 PRF-short is a 55-nt segment derived from the HIV-1 −1 PRF signal; its sequence and secondary structure are illustrated on the right, highlighted by red fonts. $(CAA)_{20}$ is an ssRNA containing 20 copies of "CAA." Representative of three independent experiments. (**D**) BLI titration of SFL against biotinylated −1 PRF-short RNA immobilized on SA biosensors. SFL concentration series used in the titration are labeled on the right. Binding kinetic parameters K_D, k_{on}, and k_{off} are shown on top. Dashed lines are the fitting of the experimental data. Representative of two independent experiments.

monomeric in solution. The higher-than-theoretical molecular mass suggests that SFL might undergo posttranslational modifications yet to be identified.

To investigate SFL-RNA interactions, we conducted electrophoretic mobility shift assays (EMSAs) using two RNA substrates (Fig. 1C). Because the complete −1 PRF signal between HIV-1 Gag-Pol (Fig. 1C, right) was too large for EMSA, we designed a 55–nucleotide (nt) truncation of the −1 PRF sequence, which included the slippery sequence and the downstream stem-loop region, denoted −1 PRF-short (Fig. 1C, right; template, NC_001802.1 1629-1683). A single-stranded 60-nt RNA $(CAA)_{20}$ containing 20 tandem copies of the CAA sequences was used as a nonspecific RNA control. Whereas SFL and −1 PRF-short formed stable complexes at the protein concentrations of 8 to 16 μM, $(CAA)_{20}$ RNA could not bind SFL at the same concentrations (Fig. 1C, left), indicating that SFL specifically recognizes the −1 PRF-short substrate. Next, we investigated binding kinetics of SFL for −1 PRF-short substrate using biolayer interferometry (BLI). Biotinylated −1 PRF-short RNA was loaded to streptavidin (SA) biosensors for binding SFL proteins supplied with a twofold serial dilution from 1 to 0.03 μM in solutions (Fig. 1D). The BLI sensorgram was recorded and analyzed using the Octet Data Analysis Software, which calculated an equilibrium dissociation constant (K_D) of 5.66 nM, indicating high affinity. The fast on-rate (k_{on}: 1.67×10^5 1/Ms) and slow off-rate (k_{off}: 9.47×10^{-4} 1/s) indicate fast RNA association and slow RNA dissociation during binding (Fig. 1D).

Crystal structure of human SFL

To explore the molecular mechanism underlying the functions of SFL, we determined the crystal structure of full-length SFL. The recombinant protein was concentrated to 4 mg/ml before crystallizing in a buffer containing 0.02 M citric acid, 0.08 M bis-tris propane (pH 8.8), and 17% (w/v) polyethylene glycol 3350. During analysis of preliminary x-ray diffraction data, we observed high anomalous

intensity differences, suggesting that SFL might contain metal ions. This is consistent with a previous study predicting a zinc finger domain within SFL (*13*). We therefore collected multiple diffraction datasets using x-rays with wavelengths 1.269 and 1.282 Å, close to the zinc absorption edge. Multiwavelength anomalous diffraction (MAD) data yielded a low-resolution electron density map (3.3 Å) and allowed building of a partial model. To improve resolution, we rescreened the crystallization conditions and identified a previously unidentified condition containing 0.2 M potassium sodium tartrate tetrahydrate and 20% (w/v) polyethylene glycol 3350 (pH 7.4). This crystal form diffracted the x-rays to 2.0-Å resolution. We then determined the final structure of SFL by molecular replacement using the partial model from MAD as the search model. We located SFL residues 1 to 277 in the final electron density map (fig. S2), with the last 14 residues at the C terminus disordered. The extreme C-terminal region contains poly-Glu segments (denoted E-rich motif), presumably causing high flexibility. Statistics of data collection and refinement are summarized in Table 1.

SFL is a boat-shaped molecule with dimensions of 77.8 Å by 51.2 Å by 35.8 Å (Fig. 2, A and B). The N-terminal portion of SFL is a distorted helical bundle (HB, α1 to α6, residues 1 to 101) fused with three zinc finger domains constituting the C-terminal portion. Zinc finger 1 (ZF1; β1 to β4, residues 104 to 140) and zinc finger 2 (ZF2; β5 to β8, residues 147 to 182) belong to the "zinc ribbon" fold group (CCCC-type) according to zinc finger domain classification (*14*). Strands β1 and β2 fold into a primary β-hairpin, on which C112 and C115 form one zinc knuckle;

Table 1. Data collection and refinement statistics. [a]*R* merge = $\Sigma_{hkl}\Sigma_j |I_{hkl,j} - I_{hkl}|/\Sigma_{hkl}\Sigma_{jhkl,j}$, where I_{hkl} is the average of symmetry-related observations of a unique reflection. [b]*R* work = $\Sigma_{hkl} ||F_{obs}(hkl)|-|F_{calc}(hkl)||/\Sigma_{hkl}|F_{obs}(hkl)|$. [c]*R* free = the cross-validation *R* factor for 5% of reflections against which the model was not refined.

	Human SFL		Human SFL (Protein Data Bank ID: 9KBO)
Data collection	**MAD phasing**		
Space group	$P2_1$		$P2_12_12$
Cell dimensions			
a, b, c (Å)	86.66, 143.47, 89.55		212.27, 89.64, 82.46
α, β, γ (°)	90.00, 94.78, 90.00		90.00, 90.00, 90.00
X-ray source	SLS X06DA		SSRF BL19U1
Wavelength (Å)	1.269 (hrem)	1.282 (peak)	0.9785
Data range (Å)	50.00–3.30	50.00–3.24	39.85–2.00
Reflections unique	64,544	67,933	70,455
R_{merge}[a] (last shell)	0.19 (1.37)	0.20 (1.29)	0.18 (1.83)
CC (1/2)	99.70 (62.00)	99.70 (66.20)	99.7 (43.7)
$I/\sigma I$	10.11 (1.25)	9.47 (1.33)	13.40 (1.60)
Completeness % (last shell)	99.60 (97.40)	99.60 (97.40)	94.4 (64.4) ellipsoidal
Redundancy (last shell)	6.94 (6.44)	6.95 (6.50)	13.10 (13.00)
Anomal Corr	27 (3)	23 (2)	2 (0)
	Refinement		
Resolution range (Å)	/	/	39.85–2.00
% Reflections in cross-validation	/	/	4.96
R_{work}[b]/R_{free}[c] (last shell)	/	/	0.24, 0.28 (0.49, 0.44)
Atoms	/	/	
All atoms	/	/	9433
Protein	/	/	8922
Zinc	/	/	12
Solvent	/	/	499
B-factors average (Å^2)	/	/	
Protein (Å2)	/	/	
Ligands (Å2)	/	/	
Solvent (Å2)	/	/	
RMSD	/	/	
Bond lengths (Å)	/	/	0.017
Bond angles (°)	/	/	1.372
Validation	/	/	
Clashscore, all atoms	/	/	10.66
% Residues in favored regions, allowed regions, outliers in Ramachandran plot	/	/	95.84, 3.88, 0.28

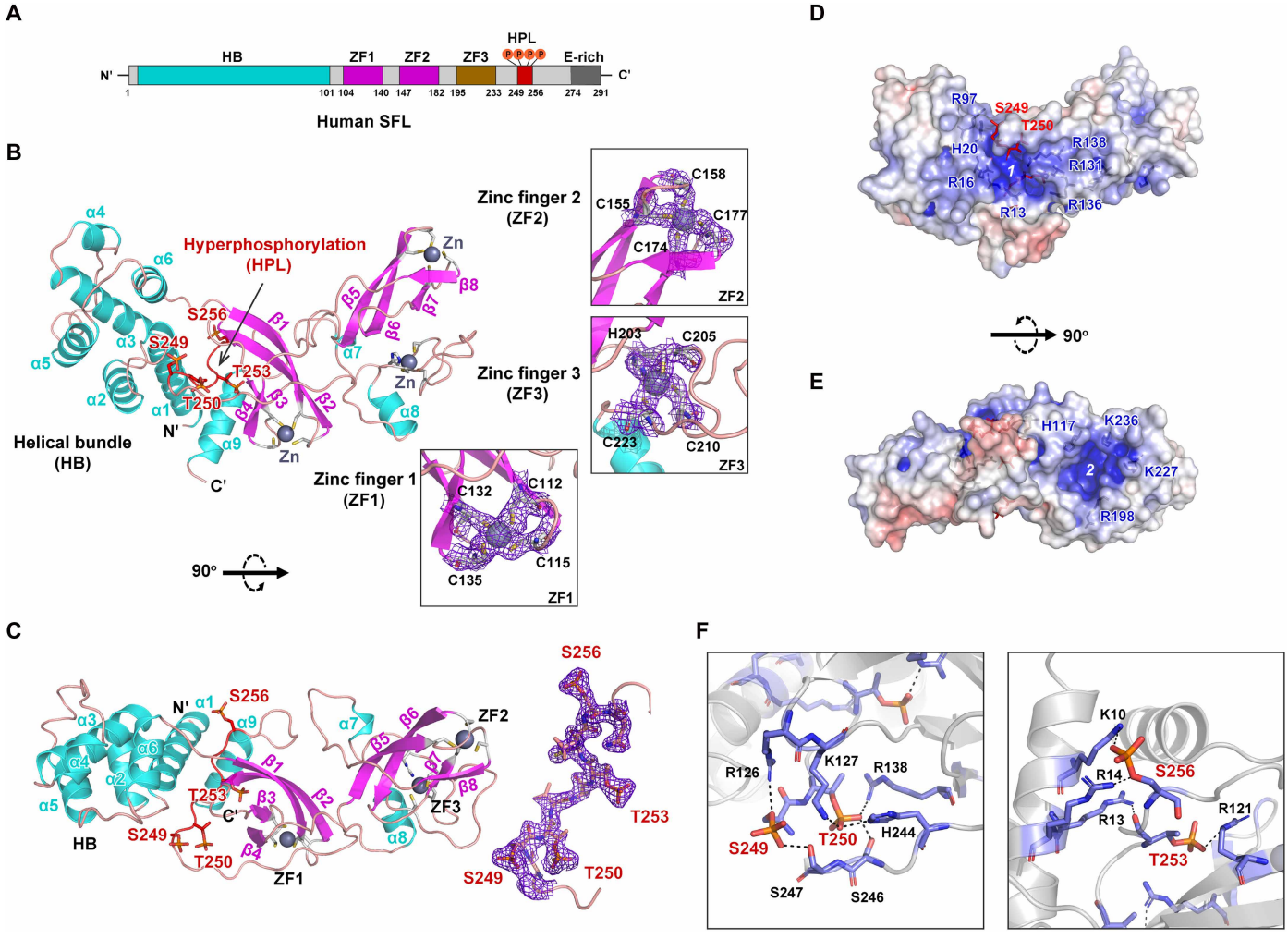

Fig. 2. Structural characterization of human SFL. (**A**) Schematics of the human SFL domain organization. SFL contains an N-terminal helical bundle domain (HB), three zinc fingers (ZF1 to ZF3), an HPL, and a C-terminal glutamate-rich domain (E-rich). (**B**) Ribbon model of human SFL with annotated secondary structures; α helices colored cyan, and β sheets colored magenta. Three zinc fingers are indicated, in which residues coordinating zinc ions are shown with stick models. Three boxes on the right are the magnified view of three zinc fingers with superimposed final $2F_o - F_c$ electron density maps (purple mesh, contour level 1.5 σ). HPL is colored red, on which phosphorylated S249, T250, T253, and S256 are shown with stick models. (**C**) Left: Bottom view of SFL (90° rotation about the horizontal axis with respect to the pose in B). Right: Stick model of HPL with superimposed final $2F_o - F_c$ electron density maps (purple mesh, contour level 1.5 σ). (**D**) Electrostatic potential surface plot of SFL; red to blue indicates negative to positive charge. Positively charged pockets 1 and 2 are identified on the SFL surface; residues constituting the positively charged pockets are shown with stick models and labeled. (**E**) 90° rotation about the horizontal axis with respect to the pose in (D). (**F**) Detailed interaction of phosphorylated S249, T250, T253, and S256 with neighboring residues; polar contacts are indicated with dashed lines.

strands β3 and β4 fold into a secondary β-hairpin, on which C132 and C135 form another zinc knuckle; the two zinc knuckles coordinate a zinc ion (Fig. 2, B and C). Likewise, strands β5 to β6 and β7 to β8 fold into two β-hairpins, on which C155 to C158 and C174 to C177 from the two zinc knuckles coordinate a zinc ion (Fig. 2, B and C). Zinc finger 3 (ZF3; residues 195 to 233) belongs to the "short zinc-binding loop" fold group (HCCC-type; Fig. 2, B and C). ZF3 lacks regular secondary structures, and the zinc ion is coordinated by three zinc-coordinating residues in close proximity in the amino acid sequence, namely, H203, C205, and C210; the fourth zinc-coordinating residue, C223, is spaced by a longer loop (Fig. 2, B and C).

We searched for structural homologs of SFL in the Protein Data Bank using the Dali server (*15*) but identified few hits. The structure of a nucleobase/ascorbic acid transporter (NAT) transporter (Protein Data Bank ID: 7TAK) had the highest *z*-score (4.9) because the NAT transporter is composed of numerous helical bundles akin to the N-terminal HB domain of SFL; however, this failed to provide useful insight into SFL functions.

We then plotted the surface electrostatic potential of the SFL structure and identified two positively charged pockets (pocket-1 and pocket-2; Fig. 2, D and E). We identified seven positively charged residues (R13, R16, H20, R97, R131, R136, and R138) in pocket-1, and four positively charge residues (H117, R198, K227, and K236) in pocket-2 (Fig. 2, D and E). The role of these positively charged pockets was investigated by mutagenesis, and the results are analyzed in the Discussion section.

In the C-terminal portion of SFL, we identified a Ser/Thr-rich loop (residues 249 to 256) between helices α8 to α9. The final

electron density map indicated that residues S249, T250, T253, and S256 on this loop were likely phosphorylated (Fig. 2C, right), suggesting that certain cellular kinases were involved in post-translational modifications. Hence, we denoted this feature the hyperphosphorylation loop (HPL). The HPL extends between the HB and the ZF1 domains where it is largely buried in the SFL core (Fig. 2C). Unexpectedly, the phosphate groups of the Ser/Thr residues are involved in multiple salt bridge interactions with the surrounding residues. For example, the phosphate group of S249 forms a salt bridge with R126; the phosphate group of T250 forms three salt bridges with K127, R138, and H244 (Fig. 2F, left); the phosphate group of T253 salt bridges with R121, and S256 salt bridges with both K10 and R14 (Fig. 2F, right). These phosphate-mediated salt bridges imply that phosphorylation plays an important role in maintaining the fold of SFL and thus affects protein functions.

SFL is phosphorylated

To confirm phosphorylation of the HPL observed in the crystal structure of SFL, we analyzed recombinant SFL using the liquid chromatography–tandem mass spectrometry (LC-MS/MS). SFL overexpressed in insect cells was treated with chymotrypsin before loading to LC-MS/MS. We achieved ~70.1% sequence coverage of SFL (fig. S3A) and identified four phosphorylation sites at S249, T250, T253, and S256 (Fig. 3, A and B), matching our observations in the electron density map (Fig. 2C, right). Multiple sequence alignment demonstrated that all four phosphorylated Ser/Thr residues are invariant from animals to humans (Fig. 3C),

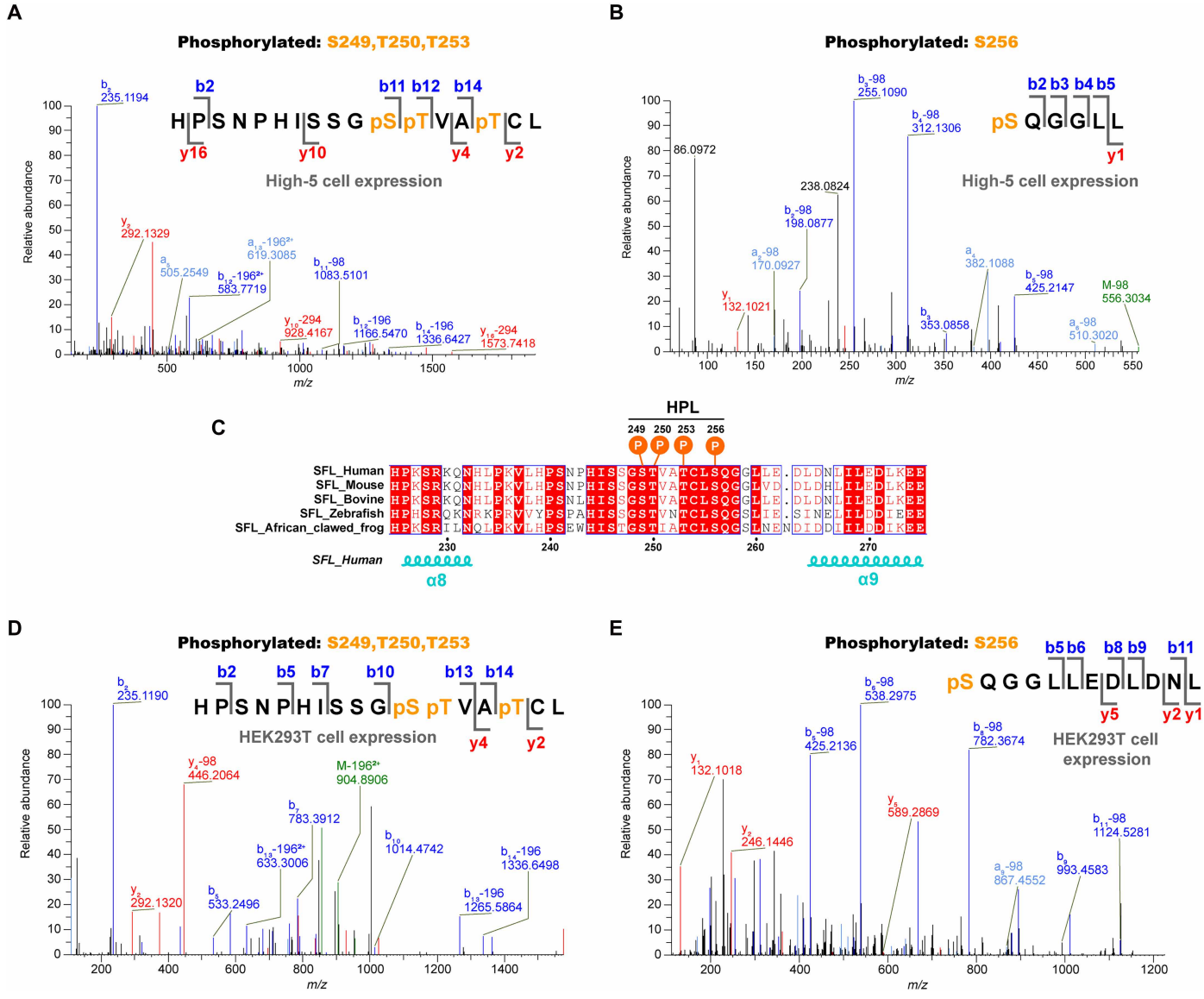

Fig. 3. Ectopically expressed SFL is phosphorylated. (**A** and **B**) LC-MS/MS spectrum of the chymotrypsinized human SFL protein ectopically expressed in high-five insect cells, which identified four phosphorylated residues, pS249, pT250, pT253, and pS256. (**C**) Multiple sequence alignment of SFL homologs from humans and various animals, which shows that four phosphorylated residues S249, T250, T253, and S256 are invariant. (**D** and **E**) LC-MS/MS spectrum of the chymotrypsinized human SFL protein ectopically expressed in HEK293F mammalian cells, which identified four phosphorylated residues, pS249, pT250, pT253, and pS256.

suggesting that the phosphorylation at HPL has been preserved during evolution. To investigate whether SFL is similarly phosphorylated in human cells, we ectopically expressed SFL in human embryonic kidney (HEK) 293F cells. Likewise, LC-MS/MS analysis of HEK293F-produced SFL (sequence coverage: ~88.8%) identified the same phosphorylation sites as observed in insect cell–derived SFL (Fig. 3, D and E, and fig. S3B). These results suggest that SFL phosphorylation may be mediated by yet-to-be-identified cellular Ser/Thr kinases, and the functional similarities between insects and humans warrant further investigation.

Phosphorylation at HPL is important for RNA binding

Because phosphorylated HPL is a highly conserved region in SFL, phosphorylation at HPL might affect functions such as RNA binding (Fig. 4). To test this postulation, we prepared four SFL mutants (S249A, T250A, T253A, and S256A), each containing

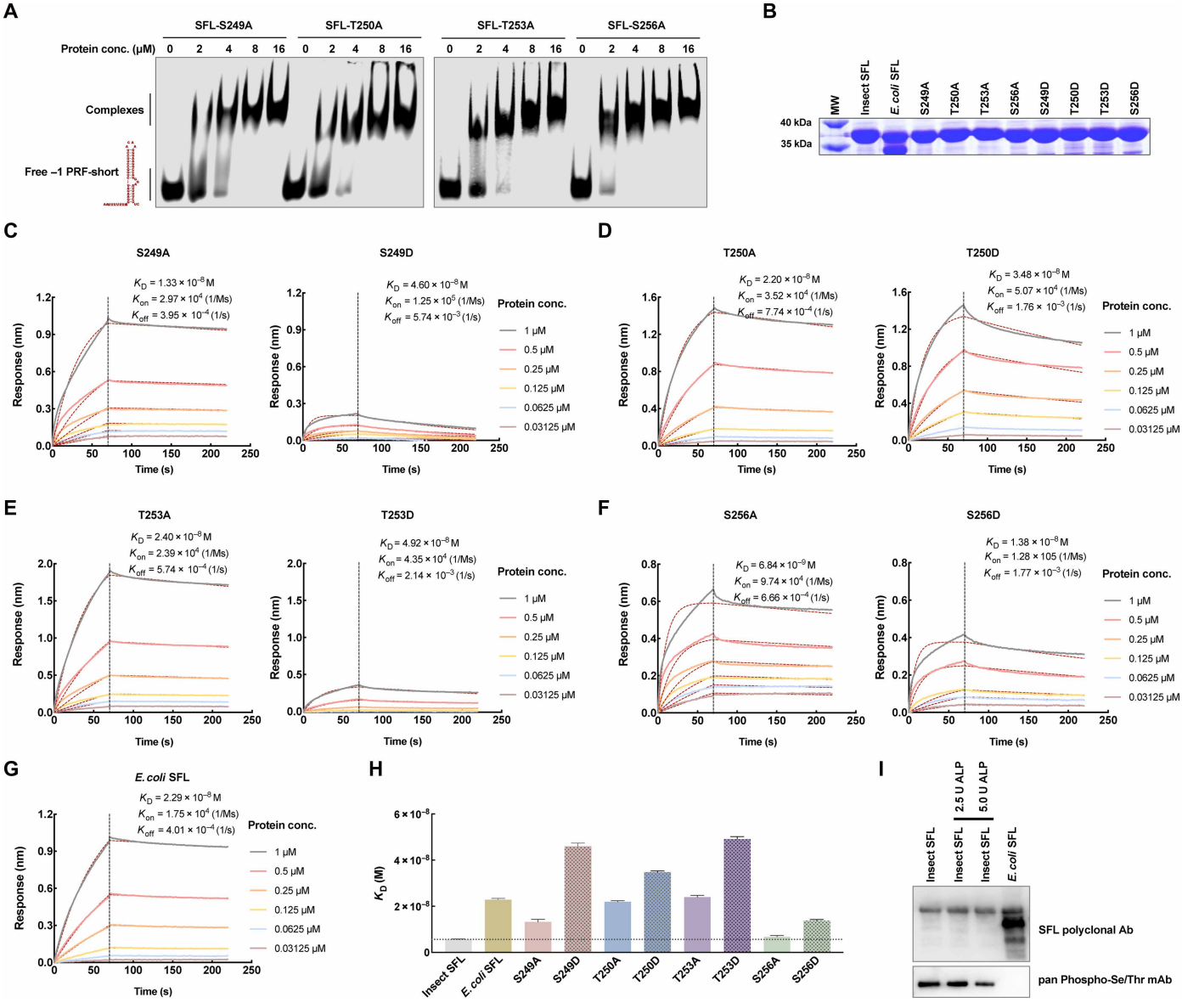

Fig. 4. Phosphorylation at HPL affects RNA binding. (**A**) EMSAs of the indicated SFL and SFL variants with the 55-nt −1 PRF-short RNA. Increasing protein concentrations used in EMSA are indicated on top of the gels. Representative of three independent experiments. (**B**) SDS-PAGE analysis of purified insect cell–expressed SFL, *E. coli*–expressed SFL, and insect cell–expressed SFL mutants S249A, T250A, T253A, S256A, S249D, T250D, T253D, and S256D. (**C** to **G**) BLI titrations of SFL mutants binding with −1 PRF-short RNA. Biotinylated −1 PRF-short RNAs were immobilized on SA biosensors for binding with SFL in solutions with a concentration series indicated on the top right. Binding kinetic parameters K_D, k_{on}, and k_{off} are shown on top of each graph. Dashed lines are the fitting of the experimental data. Representative of two independent experiments. (C) Mutants S249A and S249D. (D) Mutants T250A and T250D. (E) Mutants T253A and T253D. (F) Mutants S256A and S256D. (G) Nonphosphorylated SFL expressed from *E. coli*. (**H**) Histogram illustrating the comparison of K_D values of WT SFL and that of SFL mutants from the fitting of representative datasets. Error bars represent the fitting-derived K_D error. (**I**) Western blot analyses of insect cell–expressed SFL alone, SFL treated with ALP of different enzyme units (2.5 and 5.0 U), and *E. coli*–expressed SFL; the samples were stained with SFL pAb or pan phosphor-Ser/Thr mAb. Representative of two independent experiments.

an Ala substitution at the Ser/Thr residues in the HPL domain. The EMSA results did not clearly distinguish binding affinities (Fig. 4A); hence, we performed BLI titrations to investigate RNA binding in detail.

As shown in Fig. 4 (B to F and H) and fig. S4, the SFL mutants bearing mutation S249A, T250A, T253A, or S256A exhibited reduced binding affinity for the −1 PRF-short substrate to varying extents. Whereas S249A lost nearly half of binding affinity, the RNA binding affinities of T250A and T253A decreased more than fourfold. By contrast, the S256A mutation had negligible impact on RNA binding, with a K_D value for RNA binding similar to the wild-type (WT) SFL. The crystal structure of SFL showed that, whereas T250 and T253 are buried inside the protein core, S249 and S256 are solvent accessible (Fig. 2, B to E), and the phosphate groups of these Ser/Thr residues are involved in multiple polar contacts with the neighboring residues (Fig. 2F). To further support that phosphorylation of the HPL residues is important to −1 PRF RNA binding, we engineered additional SFL mutants containing aspartate substitutions at the HPL, namely, S249D, T250D, T253D, and S256D, which presumably mimicked the phosphorylation. To our surprise, the mutants bearing single phosphomimetic mutation all exhibited lower binding affinity for the −1 PRF RNA than those bearing the alanine substitutions (Fig. 4, B to F and H, and fig. S4). It is possible that aspartate substitutions could not fully restore the functionality of the phosphate modifications; rather, introduction of negatively charged aspartate undermined RNA binding in vitro.

Last, we investigated the binding of unphosphorylated SFL for −1 PRF RNA (Fig. 4, G to I, and fig. S4). We attempted to dephosphorylate the purified SFL from insect cell expression using alkaline phosphatase (ALP); unfortunately, ALP only dephosphorylated the insect cell–expressed SFL partially (Fig. 4I). Therefore, we expressed SFL in *Escherichia coli* and verified that the *E. coli*–expressed SFL was phosphorylation-free by Western blot (Fig. 4I) and mass spectrometry (MS) analyses (Fig. S3C). The binding affinity of unphosphorylated SFL for −1 PRF RNA reduced by ~4-fold (Fig. 4G and fig. S4), which supports that phosphorylation at HPL is important to SFL binding for −1 PRF RNA.

To investigate impact of SFL phosphorylation on binding with −1 PRF RNA using a method distinct from BLI experiments, we carried out isothermal titration calorimetry (ITC) experiments (fig. S5). Binding of SFL for HIV-1 −1 PRF RNA was an endothermic process with $\Delta H = 41.9 \pm 2.4$ kcal/mol with binding affinity $K_D = 0.39 \pm 0.08$ μM (fig. S5 and table S1). Consistent with the BLI-based experiments, four phosphorylation mutants of SFL exhibited reduced binding affinity for −1 PRF-short RNA in the ITC experiments, in which mutations T250A and T253A accounted for greater losses of binding affinity than those caused by S249A and S256A.

Collectively, these results support a hypothesis that the phosphorylation modifications at HPL are likely important for the correct folding of SFL, particularly phosphorylation of two buried residues T250 and T253.

Phosphorylation at HPL affects SFL-mediated HIV-1 inhibition

To explore whether phosphorylation at HPL plays a role in SFL-mediated −1 PRF inhibition of HIV-1 Gag-Pol, we analyzed the expression of HIV-1 proteins in HEK293T cells expressing SFL or its phosphorylation mutants (Fig. 5A). HIV-1 backbone plasmid pNL4-3.Luc.R^-.E^- was cotransfected with mammalian expression vector pcDNA3.1 harboring the coding sequence for WT SFL, SFLS, or mutant (S249A, T250A, T253A, or S256A) in HEK293T cells. Whereas expression of HIV-1 Gag-Pol was greatly inhibited by WT SFL upon overexpression, coexpression of SFLS did not reduce the Gag-Pol level, which validated the SFL-mediated −1 PRF inhibition (Fig. 5A). S-to-A mutations (S249A and S256A) at HPL preventing phosphorylation on the surface of SFL had negligible impact on −1 PRF inhibition, but T-to-A mutations (T250A and T253A) preventing phosphorylation buried in the core of SFL resulted in markedly higher HIV-1 Gag-Pol levels than with WT SFL, suggesting that phosphorylation at these two sites is more important for SFL-mediated −1 PRF inhibition (Fig. 5A). To further support this hypothesis, we engineered aspartate substitutions for T250 and T253 mimicking phosphorylation at these two sites. As anticipated, overexpression of the T250D or T253D mutant led to reduction in HIV-1 Gag-Pol level similar to that by WT SFL, indicating that the phosphomimetic mutant–mediated inhibition of −1 PRF was largely restored (Fig. 5B).

To explore the impact of SFL phosphorylation on the production of HIV-1 pseudovirus, we prepared both vesicular stomatitis virus G protein (VSV-G) pseudotyped HIV-1 particles and HIV-1 envelop (Env) pseudotyped HIV-1 particles in the presence of SFL, SFLS, or the phosphorylation mutants (Fig. 5, C and D). Whereas the VSV-G pseudotyped HIV-1 was transduced to HeLa and HEK293T cells, respectively, the HIV-1-Env pseudotyped HIV-1 was transduced to MT4 and TZM-bl cells, respectively. To our surprise, in most pseudovirus-based experiments, the SFL mutants S249A, T253A, and S256A exhibited an enhancement in the inhibition of HIV-1 pseudovirus production compared to the WT SFL; only the T250A mutant showed comparable or diminished effects (Fig. 5, C and D). It is worth noting that the mutant T250A did exhibit significantly reduced anti–HIV-1 pseudovirus activity in MT4 cells, a human T cell line physiologically relevant to HIV-1 infection.

Given that T250A and T253A mutations could abolish SFL-mediated inhibition of HIV-1 −1 PRF, but the activity of anti–HIV-1 pseudovirus production of the mutants was not severely ablated, SFL is probably involved in other anti-HIV mechanisms in addition to −1 PRF inhibition. This motivated us to investigate the SFL-mediated anti–HIV-1 activity using an authentic virus replication model (Fig. 5E). We produced replication-competent HIV-1 SG3 virus by transfecting the pSG3.1 infectious molecular clone (from S. Ghosh, B. Hahn, and G. Shaw) (*16*) into HEK293T cells. We harvested the HIV-1 SG3 viruses and determined the median tissue culture infectious dose ($TCID_{50}$) values as reported previously (*17*). We then transfected Jurkat cells with the plasmid encoding SFL (pLV-UBC-SFL-Myc-EF1a-GFP), SFLS, and SFL mutants S249A, T250A, T253A, or S256A. At 24 hours posttransfection, we infected the Jurkat cells with 200 $TCID_{50}$ HIV-1 SG3 per well and recorded virus growth curves by quantifying HIV-p24 protein from 72 to 168 hours postinfection. The virus growth curves demonstrate that, whereas WT SFL inhibited the replication of HIV-1, only mutation S256A impaired the SFL-mediated HIV-1 inhibition (Fig. 5E). By contrast, mutations S249A and T250A enhanced the SFL-mediated HIV-1 inhibition (Fig. 5E). Unexpectedly, despite being deficient in inhibiting −1 PRF, the isoform SFLS exhibited potent anti–HIV-1 activity in the authentic virus model. These results strongly suggest that SFL-mediated inhibition of −1 PRF is not directly coupled to its anti–HIV-1 activity. In other words, SFL could inhibit HIV-1 via profound mechanisms beyond −1 PRF inhibition.

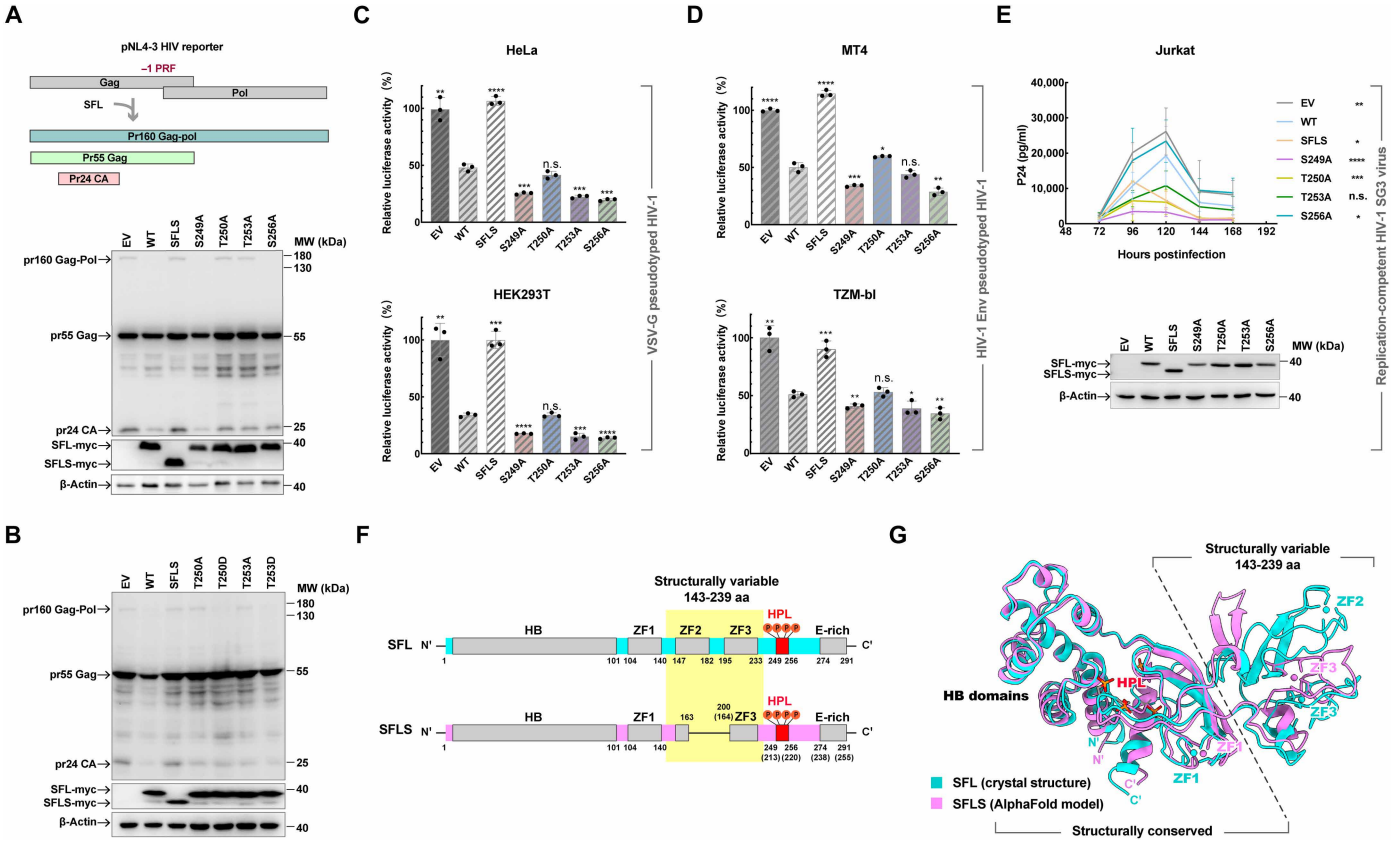

Fig. 5. Phosphorylation at HPL affects SFL-mediated HIV-1 inhibition. (**A** and **B**) Western blot analysis of HIV-1 protein expression in HEK293T cells cotransfected with an HIV-1 reporter and constructs expressing SFL, SFLS, or indicated phosphomutants. [(A), top] Diagram of HIV-1 Gag-Pol genes and production of HIV-1 proteins Pr160 GagPol (dependent on −1 PRF), Pr55 Gag, and Pr24 CA (independent of −1 PRF). Western blot of HIV-1 protein expression, SFL and SFLS and β-actin in cells expressing the SFL mutants S249A, T250A, T253A, and S256A [(A), bottom] or mutants T250A, T250D, T253A, and T253D (B). Representative of three independent experiments. (**C** and **D**) Production of VSV-G (C) and HIV-1 Env (D) pseudotyped HIV-1 in HEK293T cells expressing SFL, SFLS, or indicated phosphomutants. Virus titers were determined by transduction in HeLa [(C), top], HEK293T [(C), bottom], MT4 [(D), top], and TZM-bl [(D), bottom] cells. $n = 3$ biological replicates. (**E**) Top: HIV-1 SG3 replication in Jurkat cells expressing SFL, SFLS, or phosphomutants. Virus growth was recorded from 72 to 168 hours postinfection. Bottom: Western blot analysis of the expression of Myc-SFL and mutants. $n = 4$ biological replicates. (**F**) Diagrams of SFL and SFLS with the indicated HB domain, ZF domain, HPL domain, and E-rich domain. The structural variable region is indicated by a yellow background. aa, amino acids. (**G**) Structure superimposition of the crystal structure of SFL (cyan) with an AlphaFold model of SFLS (magenta), which reveals structurally conserved portion between two proteins comprising HB and ZF1 domains and structurally variable region comprising ZF2 and ZF3 domains. EV, empty vector. Data are presented as means ± SD. Statistical significance was determined by two-tailed unpaired *t* test [(C) and (D)] or two-way ANOVA with multiple comparisons (E) relative to WT SFL (*$P < 0.05$, **$P < 0.01$, ***$P < 0.001$, ****$P < 0.0001$; n.s., not significant).

Phosphorylation at HPL is important to SFL-mediated inhibition of −1 PRF

The −1 PRF signals are prevalent throughout all organisms, and SFL acts as a broad-spectrum inhibitor against various −1 PRFs (*2*, *5*, *12*). We therefore investigated the role of HPL phosphorylation in inhibiting different −1 PRF signals using a dual-luciferase reporter system (*2*, *18*) (Fig. 6A). Between a *Renilla* luciferase (*Rluc*) gene and a firefly luciferase (*Fluc*) gene (in the −1 frame), we inserted the −1 PRF sequences from viruses and humans, including HIV-1, human T-lymphotropic virus type 2 (HTLV-2), SARS-CoV-2, Middle East respiratory syndrome coronavirus (MERS-CoV), JEV, Chikungunya virus (CHIKV), and *PEG10* or *CCR5* genes (human). According to guidelines for the use of eukaryotic dual gene expression reporters (*19*), we engineered a positive control of the dual-luciferase −1 PRF reporter, in which an additional nucleotide was added in the slippery sequences of the −1 PRF signals, so that both Fluc and Rluc genes were translated without frameshifting (Fig. 6A, top). We engineered a negative control of the dual-luciferase −1 PRF reporter, in which a premature stop codon was added in the slippery sequences to prevent Fluc translation (Fig. 6A, top). These constructs were transfected to HEK293T cells, and the Fluc/Rluc ratio was measured to evaluate activities of various −1 PRF signals in the absence of protein factors (Fig. 6A, bottom, and fig. S6). The −1 PRF signals from various organisms exhibited different frameshift efficiencies (Fig. 6A, bottom, and fig. S6), which validated the functionality of the −1 PRF reporter systems.

Next, we measured the Fluc/Rluc ratio to assess the −1 PRF efficiency in the presence of SFL or its mutants (Fig. 6B and fig. S7). The −1 PRF from retroviruses HIV-1, HTLV-2, and CHIKV were greatly inhibited by SFL. The T-to-A mutations T250A and T253A abrogated the −1 PRF inhibition, whereas the S-to-A mutations S249A and S256A had less impact, indicating that phosphorylation at HPL is important for −1 PRF inhibition in the cases of HIV-1, HTLV-2, and CHIKV (Fig. 6B and fig. S7). Likewise, the −1 PRFs of

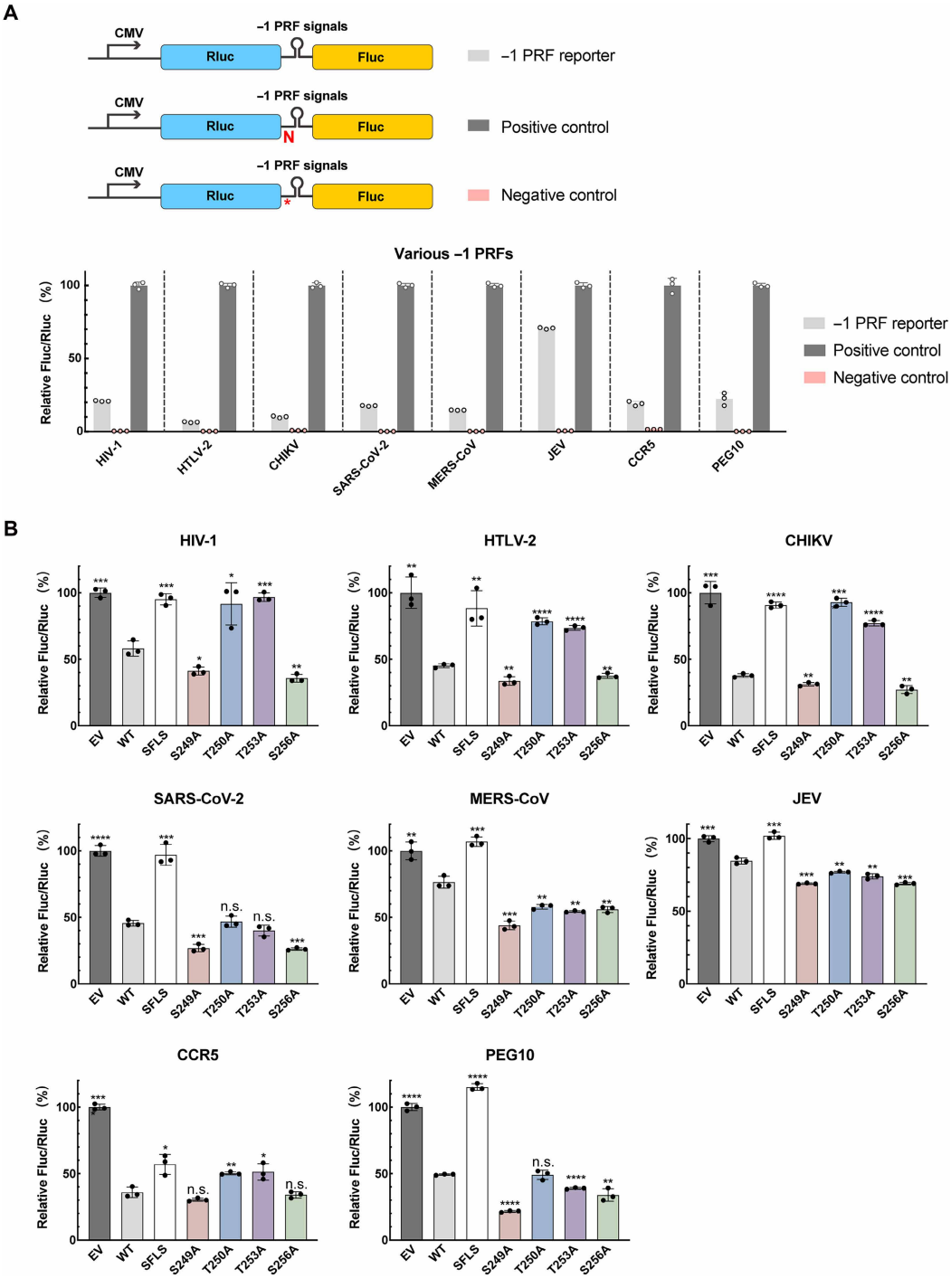

Fig. 6. Phosphorylation is important to the SFL-mediated inhibition of −1 PRF. (**A**) Diagram of the dual-luciferase reporter systems harboring indicated −1 PRF signals (bottom graph and B). The −1 PRF sequence was inserted between the *Rluc* gene and the *Fluc* gene. Positive controls of the dual-luciferase reporter systems were prepared by adding a nucleotide (indicated by a red "N") in the slippery sequence in the −1 PRF sequences; negative controls of the dual-luciferase reporter systems were prepared by adding a stop codon (indicated by a red "*") in the slippery sequence of −1 PRF. Bottom: Control experiments of the dual-luciferase reporter systems validating the activity of different −1 PRF in the absence of SFL. CMV, cytomegalovirus. All data were shown as means ± SD. $n = 3$ biological replicates. (**B**) Eight reporters contained the −1 PRF sequences from HIV-1, HTLV-2, SARS-CoV-2, MERS-CoV, JEV, CHIKV, and *PEG10* and *CCR5* genes from humans. After transfection of the indicated reporter to HEK293T cells, luciferase activities were measured to calculate the Fluc/Rluc ratio that reflects the −1 PRF efficiency mediated by SFL, SFLS, and the phosphorylation mutants. EV, empty vector. All data were shown as means ± SD. $n = 3$ biological replicates. All statistical analyses were performed relative to WT SFL and calculated using a two-tailed unpaired *t* test (*$P < 0.05$; **$P < 0.01$; ***$P < 0.001$; ****$P < 0.0001$; n.s., not significant).

coronaviruses SARS-CoV-2 and MERS-CoV, as well as the flavivirus JEV, were also inhibited by SFL, but phosphorylation at the four phosphorylation sites had minimal impact on −1 PRF inhibition (Fig. 6B and fig. S7). The −1 PRFs from human genes *CCR5* and *PEG10* were also inhibited by SFL (Fig. 6B and fig. S7). Whereas the T-to-A mutations had a significant impact on the −1 PRF of *CCR5*, the phosphorylation mutations were less effective against the −1 PRF of *PEG10* (Fig. 6B and fig. S7).

Collectively, our results suggest that phosphorylation at HPL is important for the SFL-mediated inhibition of −1 PRF activities of many organisms, if not all. In particular, the phosphorylation of Thr residues (buried) is more important than the phosphorylation of Ser residues (surface) in the cases of HIV-1, HTLV-2, and CHIKV. This is consistent with our structural characterization of SFL (Fig. 2), demonstrating that phosphorylated T250 and T253 are buried inside the SFL core and thus may be important for protein folding.

Identification of cellular kinases that phosphorylate SFL

Given that phosphorylation of SFL is important for −1 PRF inhibition, we sought to identify cellular kinases responsible for SFL phosphorylation (Fig. 7). We used a proximity-dependent biotinylation (PDB) method coupled with MS to identify the responsible kinases in living cells (*20*–*25*). We constructed three expression plasmids encoding AirID (a PDB enzyme) (*23*) and SFL-AirID fusion proteins harboring different linker regions (Fig. 6A). We engineered a short and a long linker between SFL and AirID to modulate the proximity of biotinylation (i.e., 10- and 35-nm radii, respectively; Fig. 7, A and B). At 16 hours posttransfection, HEK293T cells were lysed, and the biotinylated proteins were enriched by SA magnetic bead pulldown (Fig. 7B). Cell lysates before and after SA magnetic bead–based enrichment were analyzed by Western blot to validate the robustness and reliability of the PDB approach. The results clearly showed that, whereas SFL was efficiently enriched by SA magnetic bead pulldown, β-actin was lost (Fig. 7C).

Next, the SA bead–enriched samples were subjected to LC-MS/MS analysis. As shown in Fig. 7D, SFL was identified as the most biotinylated protein in the MS along with 27 cellular Ser/Thr kinases of 478 proteins exhibiting more than fourfold up-regulation as compared with the AirID-alone control for both 10- and 35-nm radii. To further narrow down the candidates, we used the PhosphositePlus software (*26*) to independently predict kinases responsible for the SFL phosphorylation. By combining the LC-MS/MS results with the kinase predictions (site percentile: >90%), we selected six cellular kinases, namely, EEF2K, MAP3K1, MAP3K7, NEK9, PBK, and TTK (Fig. 7E). A full list of the enriched kinases shown in Fig. 7E is provided in table S2.

To prove whether the selected kinases could phosphorylate SFL, we conducted in vitro protein kinase assays and used Phos-Tag polyacrylamide gel electrophoresis (PAGE) to analyze phosphorylated SFL species. Each of the six selected kinases was added to the protein kinase reactions containing phosphorylation-free SFL protein expressed from *E. coli* as the substrate (Fig. 7F). Comparing to control reactions without enzymes, the addition of kinase EEF2K, NEK9, or PBK kinases yielded discrete bands with markedly slower migration rates, suggesting multiple phosphorylation sites in SFL. We then excised the bands from the Phos-Tag PAGE for LC-MS/MS analysis (Fig. 7G). The sequence coverages of these bands ranged from 60 to 70% (fig. S3C). The MS data revealed that these bands were different phosphorylation forms of SFL, and the phosphorylation sites were not confined within the HPL region. In particular, EEF2K, NEK9, and PBK all phosphorylated SFL at S11 and T250, and EEF2K exhibited broader specificity than that of NEK9 and PBK, which included the phosphorylation of S249 (Fig. 7G).

To investigate the role of the phosphorylation outside of SFL HPL, we tested the impact of mutations S11A, S45A, T82A, S83A, and T88A mutations on −1 PRF activity (fig. S8). S11A, S45A, and T88A mutations significantly decreased the SFL-mediated −1 PRF inhibition, which is similar to that of T250A and T253A mutations. Notably, none of these phosphorylation sites were identified in SFL expressed in high-five insect or HEK293F mammalian cells (Fig. 3). Only S45 was predicted to be a phosphorylation site by the PhosphositePlus software. This suggests that the phosphorylation outside the HPL might be physiologically irrelevant. Even if these non-HPL sites of SFL were phosphorylated, the level of phosphorylation was too low to be detected by LC-MS/MS.

Of note, we did not identify any kinases responsible for phosphorylation at T253 and S256 of SFL, suggesting that additional cellular kinases targeting HPL remain to be identified. It is likely that our current method did not find all kinases targeting SFL. Elucidation of a comprehensive phosphoproteome of SFL is therefore important in understanding the role of phosphorylation in regulating SFL functions.

To investigate whether EEF2K, NEK9, and PBK responsible for SFL phosphorylation affect the SFL-mediated −1 PRF inhibition, we knocked down the endogenous expression of EEF2K, NEK9, or PBK in HEK293T cells. HIV-1 backbone plasmid pNL4-3.Luc.R^-.E^- was transfected to the kinase knockdown cells ectopically expressing SFL (Fig. 7H). Unfortunately, we did not observe any evident impact on the inhibitory activity of SFL. SFL-mediated inhibition of HIV-1 protein expression was largely unaffected in the absence of these kinases (Fig. 7H). The explanations could show that many cellular kinases are involved in phosphorylating SFL; thus, lack of one could be compensated by other kinases targeting the same sites.

DISCUSSION

A working model of SFL-mediated −1 PRF inhibition has been proposed previously (*2*). In the process of −1 PRF, ribosomes undergo a conformational rearrangement between their large and small subunits to create a binding interface for SFL, so that SFL can simultaneously bind the translating ribosome and a stimulatory RNA. SFL binding traps the ribosome in a nonproductive, semirotated conformation. However, experimental evidence supporting binding of SFL to ribosome and stimulatory RNA remains lacking. To unravel the molecular mechanism underlying the SFL-mediated −1 PRF inhibition, we attempted to determine the structure of SFL complexed by HIV-1 −1 PRF RNA but the intrinsic flexibility of the complex, which precluded structure determination by single-particle cryo–electron microscopy or an x-ray crystallography approach.

Previous studies indicate that SFL undergoes self-oligomerization and may exist as dimers or oligomers in solution (*2*, *11*). Nevertheless, we carried out analytical ultracentrifugation experiments and demonstrated that purified SFL formed primarily monomers in solution (Fig. 1B). It is possible that SFL oligomerization observed in previous studies involved another partner (intermediary) molecule yet to be identified.

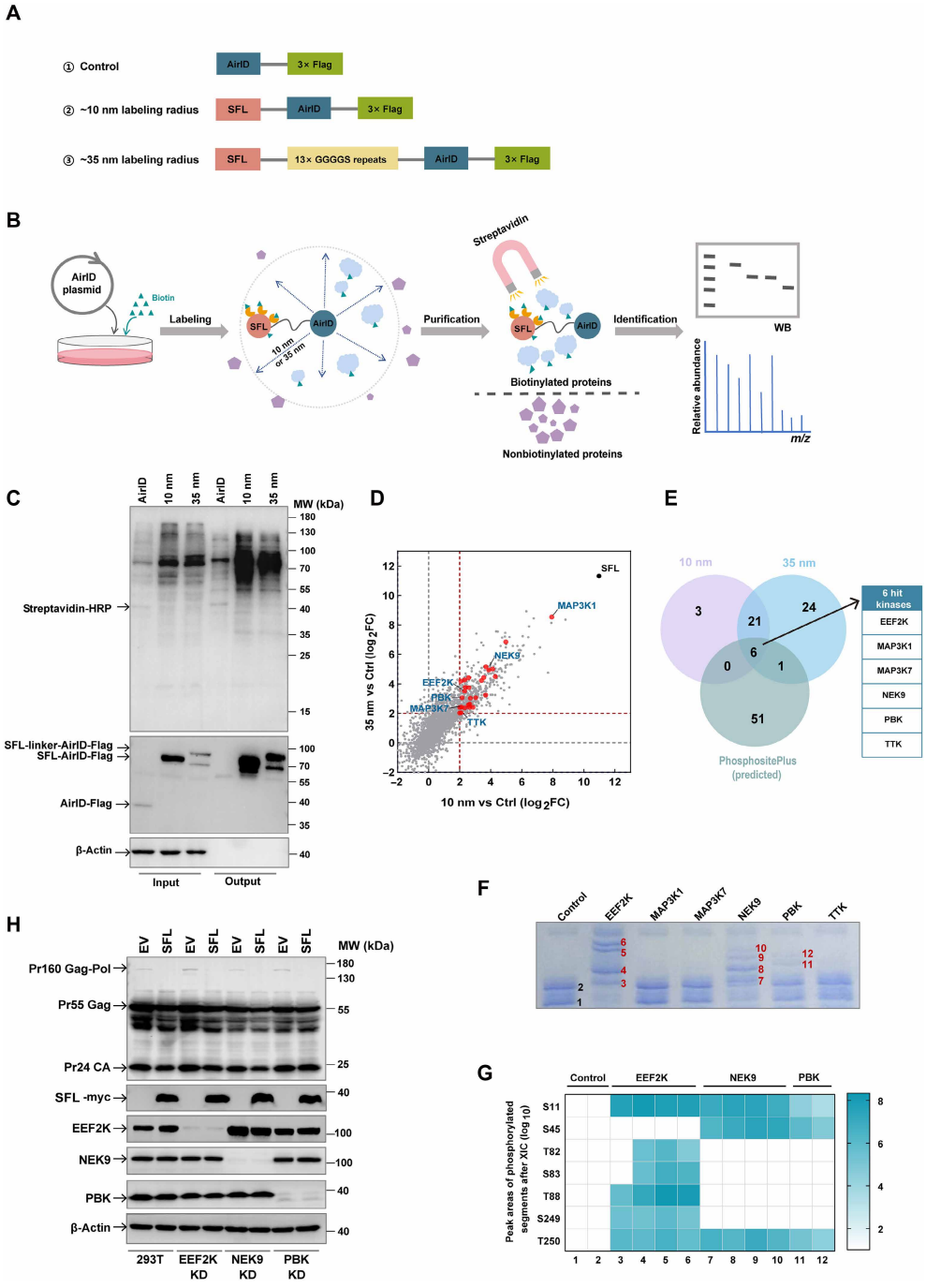

Fig. 7. Identification of kinases responsible for SFL phosphorylation. (**A**) Schematic diagram of three AirID constructs used for PDB. (**B**) Working flow of the proximity biotinylation for identifying kinases responsible for SFL phosphorylation. WB, Western blot. (**C**) The expression plasmids (A) were transfected into HEK293T cells, and 0.5 μM biotins were supplemented in the cell culture to promote biotinylation. The cells were harvested and lysed 16 hours posttransfection and analyzed by Western blot. Input: proteins before SA magnetic bead enrichment. Output: proteins after SA magnetic bead enrichment. Representative of three independent experiments. (**D**) LC-MS/MS analysis of SA magnetic bead–enriched samples from three independent biological replicates. Gray dots were proteins detected in both the 10- and 35-nm groups; black dot was SFL, and red dots were Ser/Thr kinases with expression levels at least fourfold higher than the AirID group (both 10 and 35 nm), among which six kinases (indicated with blue fonts) were selected for further analysis. FC, fold change. (**E**) Left: The purple and blue circles represent Ser/Thr kinases with expression levels up-regulated at least fourfold compared to the AirID group in the 10- and 35-nm subgroups. The green circle includes 58 kinases predicted by the PhosphositePlus software. Right: Six Ser/Thr kinases were selected because they represented the consensus of three cycles. (**F**) Phos-Tag PAGE analysis of in vitro kinase assays. Six selected kinases were tested for the ability to phosphorylate SFL. Phosphorylation species are marked by red numbers. Representative of two independent experiments. (**G**) Identification of phosphorylation sites in SFL from the marked bands in (F) by LC-MS/MS. (**H**) Expression of HIV-1 proteins in HEK293T cells with knockdown of *EEF2K*, *NEK9*, or *PBK* genes in the presence or absence of SFL. Representative of two independent experiments.

SFLS is the isoform 4 of SFL lacking a short segment (residues 164 to 199). To understand why SFLS is inactive in −1 PRF inhibition and has anti–HIV-1 activity, we compared a predicted model of SFLS (by AlphaFold 3) with the crystal structure of SFL (Fig. 5, F and G). The overall root mean square deviation (RMSD) value between the two structures was 2.6 Å, indicating structural similarity between the two isoforms. The structural comparison revealed that SFL and SFLS share a structurally conserve portion composed of the HB and ZF1 domains and a structurally variable portion composed of the ZF2 and ZF3 domains (Fig. 5, F and G). The major structural difference is that SFLS lacks the entire ZF2 domain in the structurally variable portion. We considered the zinc coordination in predicting the structure of SFLS and the model clearly revealed ZF1 and ZF3 domain with canonical fold for ion coordination. By contrast, ZF2 could not formed due to missing of zinc coordinating Cys/His residues (Fig. 5, F and G). Zinc fingers are versatile modules for interaction with nucleic acid and protein binding partners. Available experimental evidence showed that SFL can enrich RNA-containing HIV-1 Gag-pol, but SFLS cannot (*2*). Combining these results, we postulate that ZF2 of SFL presents a key module that recognizes the −1 PRF RNA sequences. Although HPL is not adjacent to ZF2, phosphorylation on HPL appears to play a regulatory role in RNA binding.

We show that both SFL and SFLS exhibited anti–HIV-1 activity (Fig. 5E) despite that SLFS did not have −1 PRF inhibition activity. It is therefore reasonable to postulate that their structurally conserved portions, i.e., the HB and ZF1 domains, might be implicated in antiviral mechanisms in addition to −1 PRF inhibition. The HB and ZF1 domains may well target critical steps in the authentic HIV-1 life cycle that were omitted in pseudovirus production. For instance, the pseudovirus packaging system used here contained an HIV-1 backbone with deficient Nef, Env, and Vpr, and the pseudovirus production did not involve the reverse transcription steps. Furthermore, Nef and Vpr play multiple roles in antagonizing host immune defense (*27*–*31*), which were also omitted in pseudovirus production. Therefore, discrepancy in the SFLS-mediated anti–HIV-1 activity observed from the pseudovirus assay (Fig. 5, C and D) and the replication-competent authentic virus assay (Fig. 5E) may stem from intrinsic differences between these assays. Unraveling anti–HIV-1 mechanism shared by SFL and SLFS warrants further investigation in the future.

Two positively charged pockets identified on the SFL surface may directly interact with RNA substrates (Fig. 2, D and E). We therefore carried out mutagenesis analysis of the positively charged residues residing in pocket-1 and pocket-2 to investigate their role in SFL-mediated −1 PRF inhibition. As illustrated in fig. S9A, five mutants (R13A, R97A, and R138A in pocket-1 and R198A and K227A in pocket-2) exhibited significantly reduced −1 PRF inhibition activity; three mutants (R16A, H20A, and R131A in pocket-1) exhibited elevated −1 PRF inhibition activity; and all other mutants were similar to WT SFL. These results suggest that both positively charged pockets are important to −1 PRF inhibition. To analyze the role of positively charged residues identified in pocket-1 and pocket-2 of SFL in −1 PRF RNA binding, we mutated each positively charge residue to alanine and produced the resulting mutants from insect cell expression. We performed BLI titrations to investigate binding affinity of −1 PRF-short RNA with SFL or its mutants. The results show that, whereas mutations R13A, R16A, H20A, and K236A resulted in losses of RNA binding affinity, the remaining mutations resulted in enhanced binding affinity (fig. S9B). Comparing the results from the −1 PRF inhibition assays (fig. S9A) and the RNA binding experiments (fig. S9B), we could not find a correlation between the −1 PRF inhibition activity and the RNA binding affinity.

It has been previously reported that SFL can inhibit viral replication via at least two mechanisms (*2*, *3*, *5*–*7*, *13*, *32*, *33*): First, it modulates cellular antiviral defenses, such as IFN responses and related signaling pathways; second, it directly interacts with viral proteins or nucleic acids to undermine virus replication, for example, by binding the viral −1 PRF sequence and thereby impairing viral protein expression. Both mechanisms are effective against viral proliferation. In this study, we demonstrate that SFL can inhibit HIV-1 through a mechanism independent of −1 PRF inhibition. This finding confirms previous research suggesting that SFL has anti–HIV-1 activity independent of the −1 PRF suppression (*11*). Further investigation is warranted to reveal other mechanisms underlying the antiviral role of SFL.

Dual-luciferase reporter experiments showed that eight distinct −1 PRF signals were regulated by SFL. Although the −1 PRF of coronaviruses, JEV, and the human *PEG10* gene were inhibited by SFL, its inhibitory activity was largely unaffected by phosphorylation of SFL (Fig. 6B). The −1 PRF sequences of HIV-1, HTLV-2, and CHIKV form stem-loop structures (*34*–*36*), whereas the −1 PRF sequences of SARS-CoV-2, MERS-CoV, JEV, and the *PEG10* gene form pseudoknot structures (*37*–*39*). Therefore, the SFL-mediated −1 PRF inhibition might be structure-specific. Availability of high-resolution SFL-RNA structures is essential to understand the mechanism underpinning −1 PRF inhibition, which warrants future structural investigation.

Phosphorylation plays vital roles in regulating gene expression; specifically, translation is regulated by the phosphorylation of initiation/elongation factors and ribosomal proteins comprising the translational complexes (*40*). SFL is also a component of the translational complexes, which is implicated in surveillance of translational fidelity and control of gene expression in cells (*41*). In the absence of virus, SFL is constitutively expressed at low levels to recognize and arrest spontaneously frameshifted ribosomes, which may assist large cellular proteins synthesis (*41*). Under viral infection SFL expression is stimulated, so that viral protein synthesis is suppressed by SFL-mediated −1 PRF inhibition. Our results provide further insights that the function SFL is modulated by phosphorylation (Figs. 5, A and B, and 6B), which implies that SFL is implicated in phosphorylation-dependent regulation of cellular and viral gene expression. Signaling pathways controlling the phosphorylation/dephosphorylation of SFL remained to be investigated.

In summary, we determined a high-resolution crystal structure of SFL and identified a hyperphosphorylation site, which was confirmed by MS. We demonstrate that phosphorylation of SFL is important for both RNA binding and the −1 PRF inhibition activity. We identified three cellular kinases responsible for SFL phosphorylation. These findings illuminate the molecular mechanism underlying the function of SFL as a broad-spectrum, highly conserved host restriction factor.

MATERIALS AND METHODS

Plasmid construction

The gene of full-length SFL (UniProtKB: Q9NUL5.2) was optimized and synthesized by GenScript. The amplified gene was then cloned

into three vectors to construct plasmids: pET28a-6×His-SUMO-SFL, pFastBac-HTB-6×His-TEV-SFL, and pcDNA3.1-6×His-SUMO-SFL, which were used to express SFL in *E. coli*, insect cells, and mammalian cells separately.

The pcDNA3.1-SFL-myc plasmids containing WT and mutant SFL were synthesized by GenScript and used for dual-luciferase assay and pseudovirus infection. The following plasmids were obtained through the NIH AIDS Reagent Program, Division of AIDS, NIAID, NIH: pNL4-3.Luc.R^-.E^- from N. Landau, pNL4-3 Env clones from D. Montefiori, and pSG3.1 molecular clone from S. Ghosh, B. Hahn, and G. Shaw. The pVSV-G plasmid encodes vesicular stomatitis virus glycoprotein and was purchased from MiaoLingBio.

In the dual-luciferase assay system, an ~100–base pair (bp) −1 PRF sequence was inserted between the Rluc gene and the Fluc gene. Only when −1 PRF occurs can the downstream Fluc be correctly expressed. Linkers (genes encoding 4×GGS) were added to both ends of the −1 PRF sequence. The plasmids pcDNA3.1-dual-luc-(−1 PRF) were synthesized by GenScript. Eight −1 PRF sequences were obtained from HIV-1, HTLV-2, SARS-CoV-2, MERS-CoV, JEV, CHIKV, and *PEG10* and *CCR5* genes from humans. The detailed −1 PRF sequence was shown in table S3, and slippery sequences were underlined. To evaluate the activity of various −1 PRF sequences and prevent false-positive signals, negative and positive controls were created using site-directed mutagenesis. To ensure that only Rluc was expressed for the negative controls, a stop codon was introduced into the slippery sequence to disrupt it. The positive controls were created by inserting a nucleotide to place both Rluc and Fluc in the same open reading frame, resulting in simultaneous production and an amino acid sequence similar to the frameshift product. The insert sequence and the pcDNA3.1-dual-luc backbone details used for construction are presented in table S3.

The pLV-UBC-SFL-Myc-EF1a-GFP plasmids containing WT and mutant *SFL* were synthesized by Beijing Tsingke Biotechnology Co. Ltd. and used for Jurkat cell transfection.

Constructing plasmids for PDB-MS, the pCMV-C-AirID-Flag vector was procured from Beyotime. Site-directed mutagenesis yielded the pCMV-AirID, enabling the expression of AirID-Flag. The *SFL* gene was polymerase chain reaction (PCR) amplified and cloned into the pCMV-C-AirID-Flag vector using Hind III and BamH I to generate pCMV-SFL-AirID-Flag. Meanwhile, the *SFL* gene was reamplified and cloned using Hind III and EcoRI to produce pCMV-SFL-13×GGGGS-AirID-Flag, incorporating a 13-repeat GGGGS sequence. All primers used in this study were listed in table S4.

Cell culture and antibodies

HEK293T [American Type Culture Collection (ATCC), CRL-1573], HeLa (Procell, CL-0101), and TZM-bl (from J. C. Kappes and X. Wu), which were obtained through the AIDS Reagent Program, Division of AIDS, NIAID, NIH, were cultured in Dulbecco's modified Eagle's medium (DMEM; Gibco, 11960-085) supplemented with 10% fetal bovine serum (FBS; Gibco, A5669701). MT4 (Procell, CL-0655) and Jurkat (Clone E6-1; ATCC, TIB-152) were cultured in RPMI 1640 medium (Gibco, C11875500BT) supplemented with 10% FBS. HEK293F (Thermo Fisher Scientific, R79007) were maintained in SMM 293-TII (Sino Biological, M293TII). High-five cells (Thermo Fisher Scientific, B85502) were cultured in EXPRESS FIVE SFM (Gibco, 10486025) supplemented with 18 mM L-Glutamine (Gibco, 25030081). *E. coli* BL21 (DE3; Thermo Fisher Scientific, EC0114) cells were grown in Luria-Bertani (LB) medium.

The antibodies used in the Western blot assay were as follows: HIV-1 p24 Rabbit monoclonal antibody (mAb) (Sino Biological, 11695-R002), Myc-Tag Mouse mAb (ABclonal, AE010), β-Actin Mouse mAb (ABclonal, AC004), SFL Rabbit polyclonal antibody (pAb) (Abcam, ab122765), pan Phospho-Serine/Threonine Mouse mAb (ABclonal, AP1067), EEF2K Rabbit pAb (Sino Biological, 207341-T36), PBK Mouse mAb (Sino Biological, 10729-MM05), NEK9 Rabbit mAb (MCE, HY-P81617), FLAG-Tag Rabbit mAb (Abcam, ab205606), horseradish peroxidase (HRP)–conjugated Goat anti-Mouse IgG (ABclonal, AS003), HRP-conjugated Goat anti-Rabbit IgG (ABclonal, AS014), and HRP-labeled Streptavidin (Beyotime, A0303).

Protein expression and purification

For biochemical experiments and crystallization, the pFastBac-HTB-6×His-TEV-SFL construct and its mutations were expressed in high-five cells using the Bac-to-Bac Baculovirus Expression System (Invitrogen). One liter of high-five cells (2.0×10^6 cells/ml) was infected with 30 ml of recombinant baculovirus at 27°C for 48 hours, and the cells were harvested at 5000*g* for 20 min. The cell pellets were resuspended in the lysis buffer [20 mM Hepes-NaOH (pH 8.0), 300 mM NaCl, and 20 mM imidazole] and lysed by sonication. After centrifugation at 47,850*g* for 60 min, the supernatant was incubated with Ni-NTA resin. The column was washed with 10 column volumes of lysis buffer, and the protein was eluted using 5 column volumes of elution buffer [20 mM Hepes-NaOH (pH 8.0), 300 mM NaCl, and 250 mM imidazole]. The 6×His tag was removed after TEV protease cleavage and reloading onto Ni-NTA resin. The protein was lastly purified by gel filtration chromatography on a Superdex 200 10/300 column (GE Healthcare) in the GF buffer containing 10 mM Hepes-NaOH (pH 8.0) and 100 mM NaCl.

To investigate the posttranslational modifications of the protein in mammals, SFL was expressed in HEK293F cells. One liter of cells (2.0×10^6 cells/ml) was transfected with 2 mg of pcDNA3.1-6×His-SUMO-SFL plasmids using polyethylenimine (6 μg/ml) at 37°C for 48 hours, and the cells were harvested at 5000*g* for 20 min. The protein purification protocols were similar to those for protein expression in high-five cells, except that, after Ni-NTA affinity chromatography, gel filtration was used directly for purification without removing the SUMO tag.

For in vitro kinase assay, construct pET28a-6×His-SUMO-SFL was expressed in *E. coli* BL21 (DE3) cells. The cells were cultured at 37°C until the optical density at 600 nm (OD_{600}) reached 0.6 to 0.8, at which point IPTG (isopropyl-β-D-thiogalactopyranoside) was added to the culture medium to a final concentration of 0.2 mM, and the cells were further cultured at 16°C for 18 hours before being harvested. The protein purification protocols were similar to those for protein expression in high-five cells, except that the 6×His-SUMO tag was cleaved using the Ulp1 protease.

Analytical ultracentrifugation

Sedimentation velocity experiments were performed in a ProteomeLab XL-I analytical ultracentrifuge (Beckman Coulter, Brea, CA), equipped with an AN-60Ti rotor (4-holes) and conventional double-sector aluminum centerpieces of 12-mm optical path length. A 380-μl solution of SFL (~0.8 mg/ml) and 400 μl of buffer [10 mM Hepes-NaOH (pH 8.0) and 100 mM NaCl] were loaded. The rotor was equilibrated for ~1 hour at 20°C before running, and then experiments were carried out at 20°C and 52,000 rpm, using continuous scan mode and radial spacing of 0.003 cm. Scans were collected

in 3-min intervals at 280 nm. The fitting of absorbance versus cell radius data was performed using the SEDFIT software and continuous sedimentation coefficient distribution c(s) model, covering a range of 0 to 15*S*.

Electrophoretic mobility shift assay

55-nt HIV-1 −1 PRF single-stranded RNA (ssRNA) "−1 PRF-short" (NC_001802.1 1629-1683) and 60-nt $(CAA)_{20}$ ssRNA were modified by CY5.5 at the 5′ terminal and synthesized by GenScript. ssRNA (0.5 μM) was incubated with 0, 2, 4, 8, and 16 μM SFL or its mutations in binding buffer [25 mM tris-HCl (pH 8.0), 100 mM NaCl, 1 mM $MgCl_2$, and 4% glycerol] for 1 hour on ice. After adding one-third volume of 4×loading buffer [50% glycerol and 2.5× tris-borate EDTA (TBE)], the electrophoresis was performed on a 6% native PAGE gel in 1×TBE buffer. The gel was visualized using Odyssey CLx (LI-COR) under the 700-nm detection channel.

Biolayer interferometry

The K_D between WT or mutant SFL and −1 PRF-short ssRNA was measured using the Octet RED96 Analysis System (ForteBio). SA biosensors were activated with phosphate-buffered saline (PBS), and then 200 nM 5' biotinylated −1 PRF-short ssRNA was annealed and loaded onto the SA biosensor. The association was performed with various concentrations of SFL or its mutants for 70 s, followed by a dissociation phase in GF buffer for 150 s. The experiment was conducted at 25°C with a shaking speed of 1000 rpm. Data analysis was performed using ForteBio Data Analysis v11.1, using a reference well subtraction method and a 1:1 model for global fitting.

Dephosphorylate the insect SFL by ALP

The reactions were performed under the following conditions: 2 μM insect SFL or *E. coli* SFL, 10 mM tris-HCl (pH 8.0 at 37°C), 5 mM $MgCl_2$, 100 mM KCl, 0.02% Triton X-100, 1 mM 2-mercaptoethanol, and bovine serum albumin (BSA; 0.1 mg/ml) with or without BalbAP Alkaline Phosphatase (Beijing BioRab, YT405). The reactions were incubated at 37°C for 60 min. The reaction samples were analyzed using Western blot.

Isothermal titration calorimetry

The binding of HIV-1 −1 PRF-short ssRNA to SFL or its mutants was carried out using MicroCal PEAQ-ITC (Malvern Panalytical, USA) at 25°C as previously described (*42*). The HIV-1 −1 PRF-short ssRNA and proteins were dissolved in GF buffer. A total of 19 consecutive 2-μl aliquots of HIV-1 −1 PRF-short ssRNA at a concentration of 50 μM in the syringe were injected into the sample cell containing 10 μM SFL or mutants at 150-s intervals with a stirring rate of 750 rpm. Data were fit to a one-site binding model using the MicroCal Origin software provided by the manufacturer.

Crystallization and structure determination

SFL expressed from high-five cells was concentrated at 4 mg/ml before crystallization. The protein was crystallized by mixing 1 μl of the sample with 1 μl of buffer containing 0.2 M potassium sodium tartrate tetrahydrate and 20% (w/v) polyethylene glycol 3350 (pH 7.4) in a hanging drop vapor diffusion system at 18°C. Crystals were flash-frozen in liquid nitrogen before measurement. The final data were collected at BL19U1 beamline of the Shanghai Synchrotron Radiation Facility (SSRF). Diffraction data were processed with the XDS package. The SFL structure was determined by molecular replacement using the software Phaser with a previously established partial model at a resolution of 3.3 Å. Manual model building was conducted using the software Coot. The crystal structure was refined using software package Phenix Data collection, and refinement parameters are summarized in Table 1.

Pseudovirus infection

The HEK293T cells were seeded in 12-well plates with 6×10^5 cells per well. After 18 hours, 500 ng of pNL4-3.Luc.R^-.E^-, 150 ng of pVSV-G or pNL4-3 Env, and 100 ng of either empty control, pcDNA3.1-SFL-myc, or SFL mutants plasmids were cotransfected into cells per well. Forty-eight hours later, the cell culture medium was centrifuged at 8000*g* for 5 min to obtain pseudoviruses. The HeLa cells or HEK293T cells were seeded in 96-well plates at a density of 4×10^4 cells per well, with 40 μl of pseudovirus solution added to each well for a 48-hour infection. To infect MT4 or TZM-bl cells, 40 μl of HIV-1 NL4-3 Env pseudovirus was introduced to each well of 96-well plates at a density of 4×10^4 cells per well for 48 hours. Then, the activity of Fluc in cells was detected according to the recommended method of Luciferase Assay System (Promega) with slight modifications. Briefly, cell lysis was first performed and lysate was transferred to a fresh 96-well opaque plate. Then, 50 μl of Luciferase Assay Reagent was added to each well and the activity of Fluc was measured using a GloMax Navigator microplate luminometer (Promega) immediately. After measurement, each sample's Fluc value was calculated by comparing to the empty vector, which was designated as 100%. All data were shown as means ± SD. The assay was performed in triplicate and repeated three times. All statistical analyses were performed relative to WT SFL and calculated using a two-tailed unpaired *t* test (*$P < 0.05$; **$P < 0.01$; ***$P < 0.001$; ****$P < 0.0001$; n.s., not significant).

Dual-luciferase assay

The activity of various −1 PFR reporters was assessed by a dual-luciferase reporter. The HEK293T cells were seeded in 96-well plates at a density of 5×10^4 cells per well. After 18 hours, Lipofectamine 2000 (Invitrogen) was used to transfect the plasmids, with 50 ng of either the −1 PRF reporter, negative control, or positive control from a different source per well. After transfection for 24 hours, the activity of Fluc and Rluc reporter genes in cells was detected according to the recommended method of Dual-Luciferase Reporter Assay System (Promega). Briefly, cell lysis was first performed, and the lysate was transferred to a fresh 96-well plate. Then, 50 μl of Luciferase Assay Reagent II containing Fluc substrate was added to each well. Immediately after, the activity of Fluc was measured using a plate reader. Then, 50 μl of Stop&Glo Reagent, containing the Rluc substrate, was added to each well. The catalytic reaction of Rluc was initiated, terminating the previous reaction, and the activity of Rluc was measured immediately. After measurement, each sample's Fluc/Rluc value was calculated relative to the corresponding positive control, which was designated as 100%. All data were shown as means ± SD. The assay was performed in triplicate and repeated three times.

The activity of SFL or its mutants was assessed to inhibit the shift of various −1 PRF reporters. The HEK293T cells were seeded in 96-well plates with 5×10^4 cells per well. After 18 hours, Lipofectamine 2000 was used to transfect the plasmids, with 50 ng of pcDNA3.1-dual-luc-(−1 PRF) and 50 ng of either empty control, pcDNA3.1-SFL-myc, or SFL mutants per well. After transfection for 24 hours,

the activity of Fluc and Rluc reporter genes in cells was detected as described above. After measurement, each sample's Fluc/Rluc value was calculated by comparing to the empty vector, which was designated as 100%. All data were shown as means ± SD. The assay was performed in triplicate and repeated three times. All statistical analyses were performed relative to WT SFL and calculated using a two-tailed unpaired *t* test (*$P < 0.05$; **$P < 0.01$; ***$P < 0.001$; ****$P < 0.0001$; n.s., not significant).

Sample preparation for PDB-MS

HEK293T cells were cultured in 10-cm dishes and allowed to reach 80% confluence. The cells were then transfected with 1.5 μg each of pcDNA3.1-AirID-Flag, pcDNA3.1-SFL-AirID-Flag, and pcDNA3.1-SFL-13×GGGGS-AirID-Flag plasmids using Lipofectamine 2000. At 5 hours posttransfection, the medium was replaced with a fresh culture medium containing 0.5 μM biotin (MCE). After 16 hours of incubation, the cells were washed twice with prechilled PBS. The cells were collected and lysed in 1 ml of radioimmunoprecipitation assay (RIPA) lysis buffer (Beyotime), followed by centrifugation at 12,000 rpm for 15 min at 4°C to obtain the cell lysate. Four percent of the lysate was separated for quality control analysis of expression and labeling by Western blot. The remaining 96% of the lysate was used to enrich biotinylated proteins. Briefly, 200 μl of Streptavidin Magnetic Beads (Beyotime) were washed three times with tris-buffered saline (TBS) buffer (Beyotime) before the addition of the lysate, and the mixture was incubated overnight at 4°C on a rotating shaker. The beads were washed five times with phosphate-buffered saline with Tween 20 (Solarbio). The beads were then resuspended in RIPA lysis buffer, and 10% of the resuspended solution was taken as the output sample for Western blot analysis. After removing the RIPA lysis buffer, the beads were washed twice with TBS buffer, and the beads were lastly stored at −80°C for subsequent LC-MS/MS analysis.

Proximity-dependent biotinylation–mass spectrometry

The sample was incubated with buffer 1 [2 M urea, 50 mM Hepes, and trypsin (0.25 μg/μl) (Promega)] at 37°C for 1 hour and buffer 2 (2 M urea and 50 mM Hepes) at 37°C for 5 min twice to elute proteins from SA magnetic beads. All supernatant was collected by centrifugation at 3000*g* for 5 min in the same tube. For digestion, proteins were reduced with 1 M dithiothreitol (DTT) for 30 min at 37°C and alkylated with 1 M indole-3-acetic acid (IAA) for 45 min at room temperature in the dark, and then trypsin (0.25 μg/μl) was added at 37°C for on-bead digestion overnight. After trypsin digestion, peptides were desalted by an SP2 column and dried by vacuum centrifuging.

All nano LC-MS/MS experiments were performed on an Orbitrap Exploris 480 (Thermo Fisher Scientific) equipped with an EASY-nLC1200 system (Thermo Fisher Scientific). Peptides were loaded onto a 100-μm inside diameter (ID)–by–8-cm trap column and separated on a 75-μm ID–by–200-mm C18 column with a 120-min linear gradient of solvent A (0.1% formic acid) and solvent B (80% acetonitrile and 0.1% formic acid). The MS analysis was performed with an Orbitrap Exploris 480 mass spectrometer (Thermo Fisher Scientific). The mass spectrometer was operated in positive mode with the FAIMS Pro interface, using data-independent acquisition (DIA) mode for high-resolution MS scans [120,000 at mass/charge ratio (*m/z*) 200] and MS/MS scans (30,000 resolution) with variable isolation windows. For nanoelectrospray ion source settings, the spray voltage was 2.2 kV; the heated capillary temperature was 320°C.

The DIA data were processed using the DIA-NN (v1.8.1) software (*43*). The protein sequence database was composed of reviewed human proteome (UP000005640_9606.fasta, 20598 entries, download date: 7 May 2024) and common contamination proteins (*44*). Trypsin (full) was specified as the proteolytic enzyme allowing up to two missed cleavages. Carbamidomethylation on Cys was specified as a fixed modification, and oxidation on Met and acetylation on protein N terminus were specified as variable modifications. The range of peptide length was set from 7 to 50. Precursor false discovery rate (FDR) was adjusted to be less than 1%. All other parameters in DIA-NN were set to their default values.

In vitro kinase assay

The kinases tested include EEF2K (MCE, HY-P701676), MAP3K1 (MERCK, SRP5047), MAP3K7 (Sino Biological, M15-13G), NEK9 (Sino Biological, N11-11G), PBK (Sino Biological, T14-10G), and TTK (MERCK, SRP5095). The reactions were performed using *E. coli*–expressed SFL as the substrate under the following conditions: 5 μM substrate, 20 nM kinase, 1 mM ATP (adenosine triphosphate), 40 mM tris-HCl, 20 mM $MgCl_2$, BSA (0.1 mg/ml), and 50 μM DTT. For the EEF2K reaction, additional components were required: calmodulin (0.03 μg/μl) and 0.5 mM $CaCl_2$. The reactions were incubated at 30°C for 90 min. The reaction samples were analyzed using Phos-tag SDS-PAGE and Coomassie blue staining.

LC-MS/MS analysis of phosphorylated SFL

Protein bands were destained overnight and dehydrated with acetonitrile until white, reduced with DTT and alkylated with iodoacetamide in the dark at room temperature, and dehydrated again, and trypsin or chymotrypsin was added for overnight digestion at 37°C. Peptides were extracted with 50% acetonitrile and 0.5% formic acid, with an additional extraction for hydrophobic peptides if expected. Extracts were dried and redissolved in 20 μl of 0.1% formic acid.

LC-MS/MS experiments were conducted on a Q Exactive Plus Bio mass spectrometer coupled with a Vanquish UHPLC system (Thermo Fisher Scientific). Peptides were resolved on an ACQUITY UPLC Peptide BEH C18 column (Waters) with a flow rate of 0.2 ml/min. The mass spectrometer operated in positive mode with a full MS scan range of 350 to 2000 *m/z* and a resolution of 70,000 and a MS/MS scan resolution of 17,500.

Data were analyzed using thee Thermo Fisher Scientific BioPharma Finder software (version 3.1) with fixed algorithm parameters. Identified peptides were screened with confidence score ≥ 90, Δ (parts per million) ≤ 15, and overall best average structural resolution ≤ 2. The extracted ion chromatogram of phosphopeptides was extracted on the basis of *m/z* values, and those with poor peak characteristics or signals below noise were recorded as 0. The XIC peak areas of all phosphopeptides at the same phosphorylation site were summed up.

CRISPR-Cas9–mediated gene knockdown

HEK293T cells with kinase knockdown were generated using commercial CRISPR-Cas9 plasmids. To achieve maximum knockdown efficiency, the CRISPR-Cas9 plasmid for each kinase consists of three plasmids transfected according to a 1:1:1 mass ratio. Each plasmid encodes the Cas9 nuclease, green fluorescent protein (GFP), and a target-specific guide RNA (gRNA). HEK293T cells were deposited in a 10-cm dish and transfected with 15 μg of EEF2K KO plasmids (Santa

Cruz Biotechnology, sc-402166), NEK9 knockout (KO) plasmids (Ubigene, YKO-RP003-hNEK9 [gRNA1], YKO-RP003-hNEK9 [gRNA2], and YKO-RP003-hNEK9 [gRNA3]), and PBK KO plasmids (Ubigene, YKO-RP003-hPBK [gRNA1], YKO-RP003-hPBK [gRNA2], and YKO-RP003-hPBK [gRNA3]) using Lipofectamine 2000, respectively. After 36 hours posttransfection, cells were collected and sorted using a BD FACSAria IIu Flow Cytometer to enrich for cells that expressed GFP successfully, and the sorted cells were expanded and cultured. The expression levels of the targeted kinases in the sorted cells were confirmed by Western blot using specific antibodies: anti-EEF2K Antibody, anti-NEK9 Antibody, and anti-PBK Antibody. Cells with confirmed gene knockdown were then used for further experiments.

Western blot analysis

HEK293T cells or HEK293T cells with a knockdown of a kinase gene were seeded in a 6-well plate. Each well was transfected with 1 μg of pNL4-3.Luc.R$^-$.E$^-$ and 1 μg of either WT or mutant pcDNA3.1-SFL-myc plasmids. After a 24-hour incubation, the cells were harvested and lysed with RIPA lysis buffer. The cell lysates were subjected to separation via 12% SDS-PAGE, after which the proteins were transferred to a 0.45-μm PVDF (polyvinylidene difluoride) membrane using a wet transfer method. The membrane was then blocked with 5% skim milk in tris-buffered saline with Tween 20 buffer at room temperature for 1 hour. Following this, the membrane was incubated with the primary antibody overnight at 4°C, washed thoroughly, and then incubated with the secondary antibody for 1 hour at room temperature. The membrane was subsequently treated with SuperSignal West Pico PLUS (Thermo Fisher Scientific) and analyzed using a ChemiDoc MP gel imager (Bio-Rad). All data are processed with Image Lab software.

Multicycle HIV-1 growth analysis

A viral stock of replication-competent HIV-1 SG3 was produced by transfecting molecular clones into HEK293T cells, as previously described (*17*). Culture supernatants were collected 48 hours posttransfection, and the $TCID_{50}$ values in TZM-bl cells were assessed. Jurkat cells were seeded in 48-well plates at 8×10^4 cells per well. Transfection was performed using ProteanFect (Nanoportal biotech) according to the manufacturer's instructions, with either empty vector control, pLV-UBC-SFL-Myc-EF1a-GFP plasmid, or its mutants. At 24 hours posttransfection, cells were infected with 200 $TCID_{50}$ of replication-competent HIV-1 SG3 virus per well and incubated at 37°C for 4 hours. After washing three times with RPMI 1640, the cells were resuspended in 200 μl of fresh culture medium and cultured at 37°C. At each indicated time point, 50 μl of the supernatant was harvested, and 50 μl of fresh medium was replenished per well. The P24 antigen in the culture supernatant was quantitated by an ELISA (enzyme-linked immunosorbent assay) kit. All data were shown as means ± SD. The assay was performed in duplicate and repeated four times. All statistical analyses were performed relative to WT SFL and calculated using a two-way analysis of variance (ANOVA) with multiple comparisons ($*P < 0.05$; $**P < 0.01$; $***P < 0.001$; $****P < 0.0001$; n.s., not significant).

Supplementary Materials

This PDF file includes:

Figs. S1 to S9
Tables S1 to S4

REFERENCES

1. H. Schmeisser, J. Mejido, C. A. Balinsky, A. N. Morrow, C. R. Clark, T. Zhao, K. C. Zoon, Identification of alpha interferon-induced genes associated with antiviral activity in Daudi cells and characterization of IFIT3 as a novel antiviral gene. *J. Virol.* **84**, 10671–10680 (2010).
2. X. Wang, Y. Xuan, Y. Han, X. Ding, K. Ye, F. Yang, P. Gao, S. P. Goff, G. Gao, Regulation of HIV-1 Gag-Pol expression by Shiftless, an inhibitor of programmed -1 ribosomal frameshifting. *Cell* **176**, 625–635.e14 (2019).
3. Y. Suzuki, W.-X. Chin, Q. E. Han, K. Ichiyama, C. H. Lee, Z. W. Eyo, H. Ebina, H. Takahashi, C. Takahashi, B. H. Tan, T. Hishiki, K. Ohba, T. Matsuyama, Y. Koyanagi, Y.-J. Tan, T. Sawasaki, J. J. H. Chu, S. G. Vasudevan, K. Sano, N. Yamamoto, Characterization of RyDEN (C19orf66) as an interferon-stimulated cellular inhibitor against dengue virus replication. *PLOS Pathog.* **12**, e1005357 (2016).
4. N. W. Hanners, K. B. Mar, I. N. Boys, J. L. Eitson, P. C. De La Cruz-Rivera, R. B. Richardson, W. Fan, M. Wight-Carter, J. W. Schoggins, Shiftless inhibits flavivirus replication in vitro and is neuroprotective in a mouse model of Zika virus pathogenesis. *Proc. Natl. Acad. Sci. U.S.A.* **118**, e2111266118 (2021).
5. D. Yu, Y. Zhao, J. Pan, X. Yang, Z. Liang, S. Xie, R. Cao, C19orf66 inhibits Japanese encephalitis virus replication by targeting −1 PRF and the NS3 protein. *Virol. Sin.* **36**, 1443–1455 (2021).
6. Y. Wu, X. Yang, Z. Yao, X. Dong, D. Zhang, Y. Hu, S. Zhang, J. Lin, J. Chen, S. An, H. Ye, S. Zhang, Z. Qiu, Z. He, M. Huang, G. Wei, X. Zhu, C19orf66 interrupts Zika virus replication by inducing lysosomal degradation of viral NS3. *PLoS Negl. Trop. Dis.* **14**, e0008083 (2020).
7. C. A. Balinsky, H. Schmeisser, A. I. Wells, S. Ganesan, T. Jin, K. Singh, K. C. Zoon, IRAV (FLJ11286), an interferon-stimulated gene with antiviral activity against dengue virus, interacts with MOV10. *J. Virol.* **91**, e00506–e00517 (2017).
8. Y. Zhang, V. Kinast, J. Sheldon, N. Frericks, D. Todt, M. Zimmer, N. Caliskan, R. J. P. Brown, E. Steinmann, T. Pietschmann, Mouse liver-expressed Shiftless is an evolutionarily conserved antiviral effector restricting human and murine Hepaciviruses. *Microbiol. Spectr.* **11**, e0128423 (2023).
9. N. Jäger, S. Pöhlmann, M. V. Rodnina, S. A. Ayyub, Interferon-stimulated genes that target retrovirus translation. *Viruses* **16**, 933 (2024).
10. N. Jäger, S. A. Ayyub, N. Korniy, F. Peske, M. Hoffmann, M. V. Rodnina, S. Pöhlmann, Mutagenic analysis of the HIV restriction factor Shiftless. *Viruses* **14**, 1454 (2022).
11. N. Jäger, S. A. Ayyub, F. Peske, D. Liedtke, J. Bohne, M. Hoffmann, M. V. Rodnina, S. Pöhlmann, The inhibition of Gag-Pol expression by the restriction factor Shiftless is dispensable for the restriction of HIV-1 infection. *Viruses* **16**, 583 (2024).
12. N. Schmidt, C. A. Lareau, H. Keshishian, S. Ganskih, C. Schneider, T. Hennig, R. Melanson, S. Werner, Y. Wei, M. Zimmer, J. Ade, L. Kirschner, S. Zielinski, L. Dölken, E. S. Lander, N. Caliskan, U. Fischer, J. Vogel, S. A. Carr, J. Bodem, M. Munschauer, The SARS-CoV-2 RNA–protein interactome in infected human cells. *Nat. Microbiol.* **6**, 339–353 (2021).
13. V. Kinast, A. Plociennikowska, Anggakusuma, T. Bracht, D. Todt, R. J. P. Brown, T. Boldanova, Y. Zhang, Y. Brüggemann, M. Friesland, M. Engelmann, G. Vieyres, R. Broering, F. W. R. Vondran, M. H. Heim, B. Sitek, R. Bartenschlager, T. Pietschmann, E. Steinmann, C19orf66 is an interferon-induced inhibitor of HCV replication that restricts formation of the viral replication organelle. *J. Hepatol.* **73**, 549–558 (2020).
14. S. S. Krishna, I. Majumdar, N. V. Grishin, Structural classification of zinc fingers: Survey and summary. *Nucleic Acids Res.* **31**, 532–550 (2003).
15. L. Holm, L. M. Laakso, Dali server update. *Nucleic Acids Res.* **44**, W351–W355 (2016).
16. S. K. Ghosh, P. N. Fultz, E. Keddie, M. S. Saag, P. M. Sharp, B. H. Hahn, G. M. Shaw, A molecular clone of HIV-1 tropic and cytopathic for human and chimpanzee lymphocytes. *Virology* **194**, 858–864 (1993).
17. H. Chong, J. Xue, Y. Zhu, Z. Cong, T. Chen, Q. Wei, C. Qin, Y. He, Monotherapy with a low-dose lipopeptide HIV fusion inhibitor maintains long-term viral suppression in rhesus macaques. *PLOS Pathog.* **15**, e1007552 (2019).
18. J. A. Kelly, M. T. Woodside, J. D. Dinman, Programmed −1 ribosomal frameshifting in coronaviruses: A therapeutic target. *Virology* **554**, 75–82 (2021).
19. G. Loughran, D. E. Andreev, I. M. Terenin, O. Namy, M. Mikl, M. M. Yordanova, C. J. McManus, A. E. Firth, J. F. Atkins, C. S. Fraser, Z. Ignatova, S. Iwasaki, J. Kufel, O. Larsson, S. A. Leidel, A. S. Mankin, M. Mariotti, M. E. Tanenbaum, I. Topisirovic, N. Vazquez-Laslop, G. Viero, N. Caliskan, Y. Chen, P. L. Clark, J. D. Dinman, P. J. Farabaugh, W. V. Gilbert, P. Ivanov, J. S. Kieft, O. Muhlemann, M. S. Sachs, I. N. Shatsky, N. Sonenberg, A. L. Steckelberg, A. E. Willis, M. T. Woodside, L. S. Valasek, S. E. Dmitriev, P. V. Baranov, Guidelines for minimal reporting requirements, design and interpretation of experiments involving the use of eukaryotic dual gene expression reporters (MINDR). *Nat. Struct. Mol. Biol.* **32**, 418–430 (2025).
20. D. I. Kim, B. Kc, W. Zhu, K. Motamedchaboki, V. Doye, K. J. Roux, Probing nuclear pore complex architecture with proximity-dependent biotinylation. *Proc. Natl. Acad. Sci. U.S.A.* **111**, E2453–E2461 (2014).

21. R. Varnaitė, S. A. MacNeill, Meet the neighbors: Mapping local protein interactomes by proximity-dependent labeling with BioID. *Proteomics* **16**, 2503–2518 (2016).
22. T. C. Branon, J. A. Bosch, A. D. Sanchez, N. D. Udeshi, T. Svinkina, S. A. Carr, J. L. Feldman, N. Perrimon, A. Y. Ting, Efficient proximity labeling in living cells and organisms with TurboID. *Nat. Biotechnol.* **36**, 880–887 (2018).
23. K. Kido, S. Yamanaka, S. Nakano, K. Motani, S. Shinohara, A. Nozawa, H. Kosako, S. Ito, T. Sawasaki, AirID, a novel proximity biotinylation enzyme, for analysis of protein–protein interactions. *Elife* **9**, e54983 (2020).
24. R. Inoue, Y. Fukutani, T. Niwa, H. Matsunami, M. Yohda, Identification and characterization of proteins that are involved in RTP1S-dependent transport of olfactory receptors. *Int. J. Mol. Sci.* **24**, 7829 (2023).
25. D. I. Kim, S. C. Jensen, K. A. Noble, B. Kc, K. H. Roux, K. Motamedchaboki, K. J. Roux, Y. Zheng, An improved smaller biotin ligase for BioID proximity labeling. *Mol. Biol. Cell* **27**, 1188–1196 (2016).
26. J. L. Johnson, T. M. Yaron, E. M. Huntsman, A. Kerelsky, J. Song, A. Regev, T.-Y. Lin, K. Liberatore, D. M. Cizin, B. M. Cohen, N. Vasan, Y. Ma, K. Krismer, J. T. Robles, B. van de Kooij, A. E. van Vlimmeren, N. Andrée-Busch, N. F. Käufer, M. V. Dorovkov, A. G. Ryazanov, Y. Takagi, E. R. Kastenhuber, M. D. Goncalves, B. D. Hopkins, O. Elemento, D. J. Taatjes, A. Maucuer, A. Yamashita, A. Degterev, M. Uduman, J. Lu, S. D. Landry, B. Zhang, I. Cossentino, R. Linding, J. Blenis, P. V. Hornbeck, B. E. Turk, M. B. Yaffe, L. C. Cantley, An atlas of substrate specificities for the human serine/threonine kinome. *Nature* **613**, 759–766 (2023).
27. A. Simmons, V. Aluvihare, A. McMichael, Nef triggers a transcriptional program in T cells imitating single-signal T cell activation and inducing HIV virulence mediators. *Immunity* **14**, 763–777 (2001).
28. E. N. Pawlak, J. D. Dikeakos, HIV-1 Nef: A master manipulator of the membrane trafficking machinery mediating immune evasion. *Biochim. Biophys. Acta* **1850**, 733–741 (2015).
29. M. E. González, The HIV-1 Vpr protein: A multifaceted target for therapeutic intervention. *Int. J. Mol. Sci.* **18**, 126 (2017).
30. J. M. Gibbons, K. M. Marno, R. Pike, W. J. Lee, C. E. Jones, B. W. Ogunkolade, C. Pardieu, A. Bryan, R. M. Fu, G. Warnes, P. A. Rowley, R. D. Sloan, Á. McKnight, HIV-1 accessory protein Vpr interacts with REAF/RPRD2 to mitigate its antiviral activity. *J. Virol.* **94**, e01591-19 (2020).
31. M. Emerman, HIV-1, Vpr and the cell cycle. *Curr. Biol.* **6**, 1096–1103 (1996).
32. W. Rodriguez, K. Srivastav, M. Muller, C19ORF66 broadly escapes virus-induced endonuclease cleavage and restricts Kaposi's sarcoma-associated herpesvirus. *J. Virol.* **93**, e00373–e00319 (2019).
33. H. Wang, N. Kong, Y. Jiao, S. Dong, D. Sun, X. Chen, H. Zheng, W. Tong, H. Yu, L. Yu, W. Zhang, G. Tong, T. Shan, EGR1 suppresses porcine epidemic diarrhea virus replication by regulating IRAV to degrade viral nucleocapsid protein. *J. Virol.* **95**, e00645-21 (2021).
34. Y. G. Kim, S. Maas, A. Rich, Comparative mutational analysis of cis-acting RNA signals for translational frameshifting in HIV-1 and HTLV-2. *Nucleic Acids Res.* **29**, 1125–1131 (2001).
35. D. Dulude, M. Baril, L. Brakier-Gingras, Characterization of the frameshift stimulatory signal controlling a programmed –1 ribosomal frameshift in the human immunodeficiency virus type 1. *Nucleic Acids Res.* **30**, 5094–5102 (2002).
36. J. A. Kendra, V. M. Advani, B. Chen, J. W. Briggs, J. Zhu, H. J. Bress, S. M. Pathy, J. D. Dinman, Functional and structural characterization of the chikungunya virus translational recoding signals. *J. Biol. Chem.* **293**, 17536–17545 (2018).
37. P. R. Bhatt, A. Scaiola, G. Loughran, M. Leibundgut, A. Kratzel, R. Meurs, R. Dreos, K. M. O'Connor, A. McMillan, J. W. Bode, V. Thiel, D. Gatfield, J. F. Atkins, N. Ban, Structural basis of ribosomal frameshifting during translation of the SARS-CoV-2 RNA genome. *Science* **372**, 1306–1313 (2021).
38. T. S. Cardno, Y. Shimaki, B. E. Sleebs, K. Lackovic, J. P. Parisot, R. M. Moss, C. Crowe-McAuliffe, S. F. Mathew, C. D. Edgar, T. Kleffmann, W. P. Tate, HIV-1 and human PEG10 frameshift elements are functionally distinct and distinguished by novel small molecule modulators. *PLOS ONE* **10**, e0139036 (2015).
39. A. E. Firth, J. F. Atkins, A conserved predicted pseudoknot in the NS2A-encoding sequence of West Nile and Japanese encephalitis flaviviruses suggests NS1′ may derive from ribosomal frameshifting. *Virol. J.* **6**, 14 (2009).
40. J. W. Hershey, Overview: Phosphorylation and translation control. *Enzyme* **44**, 17–27 (1990).
41. J. A. Kelly, J. D. Dinman, Shiftless is a novel member of the ribosome stress surveillance machinery that has evolved to play a role in innate immunity and cancer surveillance. *Viruses* **15**, 2296 (2023).
42. K. Zhu, L. Song, L. Wang, L. Hua, Z. Luo, T. Wang, B. Qin, S. Yuan, X. Gao, W. Mi, S. Cui, SARS-CoV-2 ORF10 hijacking ubiquitination machinery reveals potential unique drug targeting sites. *Acta Pharm. Sin. B* **14**, 4164–4173 (2024).
43. V. Demichev, C. B. Messner, S. I. Vernardis, K. S. Lilley, M. Ralser, DIA-NN: Neural networks and interference correction enable deep proteome coverage in high throughput. *Nat. Methods* **17**, 41–44 (2020).
44. S. Tyanova, T. Temu, J. Cox, The MaxQuant computational platform for mass spectrometry-based shotgun proteomics. *Nat. Protoc.* **11**, 2301–2319 (2016).

Acknowledgments: Flow cytometry experiments were conducted at the Core Facilities and Service Centers, NIPB, and CAMS&PUMC. We thank L. Li and Y. Xiao for expert assistance with flow cytometry experiments and ITC analysis. We thank M. Wang and the staff of the Swiss Light Source group for macromolecular crystallography at the Paul Scherrer Institute (Villigen, Switzerland) for assistance in data collection. We thank the staff of BL19U1 beamline of the National Facility for Protein Science in Shanghai (NFPS) at the Shanghai Synchrotron Radiation Facility (SSRF) for assistance during data collection. We thank J. Fu and N. Zhai in the core facility of the First Hospital of Jilin University for the guidance on MS data analysis. **Funding:** This work was supported by the National Key Research and Development Program of China (2023YFC2307800, to S.C.), CAMS Innovation Fund for Medical Sciences (2021-I2M-1-037, to S.C.; 2021-I2M-1-043, to Z. Li; and 2023-I2M-2-001, to S.C.), the Non-profit Central Research Institute Fund of Chinese Academy of Medical Sciences (2023-PT310-04, to S.C.; 2023-PT330-01, to S.C.), and National Natural Science Foundation of China (82341095, to S.C.; 82261160398, to S.C.; and 82402596, to B.Q.). **Author contributions:** Conceptualization: Z. Li and S.C. Methodology: Y.Z., Z. Li, H.C., P.H., W.H., Z. Liu, W.J., Y.H., and S.C. Software: Z. Liu and W.J. Validation: Y.Z., Z. Li, H.C., P.H., M.L., and S.C. Formal analysis: Y.Z., Z. Li, H.C., Z. Liu, W.J., B.Q., Y.H., and S.C. Investigation: Y.Z., Z. Li, H.C., P.H., W.H., Y.H., and S.C. Resources: H.C., W.H., Z. Liu, Y.H., and S.C. Data curation: Z. Li, Z. Liu, Y.H., and S.C. Writing—original draft: Y.Z., Z. Li, Z. Liu, and S.C. Writing—review and editing: Y.Z., Z. Li, H.C., and S.C. Visualization: Y.Z., Z. Li, and S.C. Supervision: Z. Li, Y.H., and S.C. Project administration: Z. Li, Y.H., and S.C. Funding acquisition: Z. Li, B.Q., and S.C. **Competing interests:** The authors declare that they have no competing interests. **Data and materials availability:** All data and code needed to evaluate and reproduce the results in the paper are present in the paper and/or the Supplementary Materials. Coordinates and structure factors are deposited in the Protein Data Bank with ID: 9KBO.

Submitted 14 February 2025
Accepted 19 November 2025
Published 19 December 2025
10.1126/sciadv.adw7471

ScienceAdvances

Phosphorylation of shiftless is important for inhibiting the programmed #1 ribosomal frameshift

Yueli Zhang, Zhijian Li, Huihui Chong, Pengjiao Hou, Wei Hao, Mengyun Li, Zhicheng Liu, Wei Jia, Bo Qin, Yuxian He, and Sheng Cui

Sci. Adv. **11** (51), eadw7471. DOI: 10.1126/sciadv.adw7471